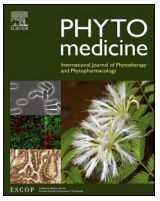
Phytomedicine 158 (2026) 158349



Contents lists available at ScienceDirect

Phytomedicine

journal homepage: www.elsevier.com/locate/phymed



Original Article



Deciphering the complex mechanisms of action of lead detoxification by the green microalga *Chlorella vulgaris*

Chunmei Jin [a], Seren Gündoğdu [a,b], Nesrine M. Hegazi [c], Xiaohua Lu [a], Mohamed Elbadawi [a], Christopher Kampf [d], Sabine M Klauck [e], Sarra Rahali [d], Nico Achenbach [d], Mohamed-Elamir F. Hegazy [a,f], Thomas Efferth [a,*]

[a] *Department of Pharmaceutical Biology, Institute of Pharmaceutical and Biomedical Sciences, Johannes Gutenberg University, Staudinger Weg 5, 55128 Mainz, Germany*
[b] *Department of Pharmacognosy, Faculty of Pharmacy, Hacettepe University, Ankara 06100, Türkiye*
[c] *Phytochemistry and Plant Systematics Department, National Research Centre, 33 El-Bohouth St., Dokki, Giza 12622, Egypt*
[d] *Department of Chemistry, Johannes Gutenberg University, Duesbergweg 10-14, 55128 Mainz, Germany*
[e] *Division of Cancer Genome Research, German Cancer Research Center (DKFZ), Heidelberg, National Center for Tumor Diseases (NCT), NCT Heidelberg, a Partnership between DKFZ and University Hospital Heidelberg, Im Neuenheimer Feld 280, 69120 Heidelberg, Germany*
[f] *Chemistry of Medicinal Plants Department, National Research Centre, 33 El-Bohouth St., Dokki, 12622 Giza, Egypt*

ARTICLE INFO

Keywords:
Algal extract
Heavy metal
DMT1
Ferroptosis
Poisoning
Toxicity

ABSTRACT

Background: Lead (Pb) intoxication necessitates detoxification strategies that are efficacious and devoid of the adverse effects characteristic of synthetic chelators. The green microalga *Chlorella* is of particular interest because it exerts diverse metal-binding properties and is rich in micronutrients that collectively support detoxification with a potentially more favorable safety profile.
Hypothesis: We hypothesized that employing an experimental model with enhanced Pb^{2+} transport capacity by cells transfected with a cDNA encoding the divalent metal transporter 1 (DMT1) and a *Chlorella* dietary supplement could help elucidate the specific mechanisms underlying its detoxification action.
Methods: To identify the optimal species, the extracts from *Chlorella vulgaris* (*C. vulgaris*) *and Chlorella pyrenoidosa* (*C. pyrenoidosa*) supplements were compared in metabolomic profiling by HPLC-HRMS/MS. The DMT1-overexpressing cell model was constructed by assessing the detoxification efficacy of *C. vulgaris* extract using cell viability and the Trolox equivalent antioxidant capacity assays. Pb^{2+} concentration was measured by Inductively Coupled Plasma Optical Emission Spectrometry (ICP-OES). To map the complex mechanisms of

Abbreviations: ALAD, δ-aminolevulinic acid dehydratase; ANAPC4, Anaphase promoting complex subunit 4; ARID3B, AT-rich interaction domain 3B; ATP, Adenosine triphosphate; ATP6V0A2, ATPase H+ transporting V0 subunit A2; ATP7B, ATPase copper transporting beta; Bcl-xL, B-cell lymphoma-extra-large; CaNa$_2$EDTA, Sodium-calcium-ethylenediaminetetraacetic acid; CGF, *Chlorella* growth factor; CHO, Chinese hamster ovary; CNGB4, Cyclic nucleotide gated channel subunit beta 4; *C pyrenoidosa* or CP-J, *Chlorella pyrenoidosa*; CTSB, Cathepsin B; *C vulgaris* or CV, *Chlorella vulgaris*; DEGs, Differentially expressed genes; DFO, Deferoxamine; DGMG, Diglycosidic monacyl glycerols; DLAT, Dihydrolipoamide S-acetyltransferase; DMSA, Meso-2,3-dimercaptosuccinic acid; DMT1, Divalent metal transporter 1; ERK, Extracellular signal-regulated kinase; FDX1, Ferredoxin 1; FTH1, Ferritin heavy chain 1; HIF-1α, Hypoxia-inducible factor 1α; HMOX1, Heme oxygenase 1; ICAM1, Intercellular adhesion molecule 1; JNK, c-Jun N-terminal kinase; KCNF1, Potassium voltage-gated channel modifier subfamily F member 1; LC3B, Microtubule-associated proteins 1A/1B light chain 3 beta; LIAS, Lipoic acid synthetase; L-2-HG, L-2-hydroxyglutarate; MDH, Malate dehydrogenase; MGMG, Monoglycosidic monoacyl glycerols; MTs, Metallothioneins; MSCs, Mesenchymal stem cells; NCOA4, Nuclear receptor coactivator 4; NF-κB, Nuclear factor kappa B subunit; p62, Sequestosome-1; p38 MAPK, Mitogen-activated protein kinase; PARP, Poly [ADP-ribose] polymerase; PCs, Phosphatidylcholines; PEs, Phosphatidylethanolamines; PGs, Phosphatidylglycerols; PHC3, Polyhomeotic homolog 3; PHDs, Prolyl-hydroxylases; PI3K, Phosphoinositide 3-kinase; PIs, Phosphatidylinositols; RELA, RELA proto-oncogene, NF-KB subunit; SLC7A11, Solute carrier family 7 member 11; SLC16A1, Solute carrier family 16 member 1; STAT3, Signal transducer and activator of transcription 3; TASOR2, Translocation-associated sensor Of RAS homolog 2; TFR2, Transferrin receptor 2; TIPARP, TCDD inducible poly(ADP-ribose) polymerase; TMEM175, Transmembrane protein 175; TOR2A, Torsin family 2 member A; TSG101, Tumor susceptibility 101; VPS26A, VPS26, retromer complex component A; XRCC5, X-ray repair cross complementing 5; ZFPs, Zinc finger proteins; ZNF205, Zinc finger protein 205, ZNF217, zinc finger protein 217; α-KG, α-ketoglutarate.

* Corresponding author.
E-mail address: efferth@uni-mainz.de (T. Efferth).

https://doi.org/10.1016/j.phymed.2026.158349
Received 10 March 2026; Received in revised form 18 May 2026; Accepted 23 May 2026
Available online 28 May 2026
0944-7113/© 2026 The Authors. Published by Elsevier GmbH. This is an open access article under the CC BY license (http://creativecommons.org/licenses/by/4.0/).

action, transcriptomic analyses were performed and analyzed using Ingenuity Pathway Analysis (IPA) and validated by western blotting and fluorescence microscopy.
Results: Metabolite profiling and antioxidant capacity assay identified the *C. vulgaris* aqueous extract as superior. It attenuated Pb^{2+}-induced cytotoxicity and was prone to promote cellular Pb^{2+} export in DMT1-transfected cells. Transcriptomics revealed that Pb^{2+} exhibited a signature of hepatorenal toxicity, and the aqueous extract rescued the zinc finger protein's function. Western blot and fluorescence microscopy validated that *C. vulgaris* water extract may orchestrate a multifaceted defense: rectifying Pb^{2+}-induced autophagic flux blockage, alleviating ferroptotic stress, triggering an adaptive metabolic shift via protein lipoylation and a p-STAT3-mediated survival pathway, jointly preserving microtubule integrity.
Conclusion: These findings advance prior research by first providing a comprehensive detoxification mechanism framework of *C. vulgaris*, positioning *C. vulgaris* as a promising, multi-mechanism supplement for mitigating Pb^{2+} poisoning.

Introduction

Lead poisoning remains a critical public issue, classified by the WHO among the ten chemicals of major public health concern. The widespread anthropogenic contamination of lead, originating from gasoline additive (tetraethyllead, since 1923), has made it persistent in environmental matrices. At the cellular level, lead exerts its toxicity through interconnected mechanistic pathways centered on oxidative stress, cation mimicry, and mitochondrial dysfunction (Thakur et al., 2025). Despite its redox stability (Soria-Aguilar et al., 2021), it cannot directly generate reactive oxygen species (ROS) like transition metals (*e.g.*, Fe^{2+}, Cu^{+}) via Fenton/Haber-Weiss reactions (Kanti Das et al., 2014), Pb^{2+} potently amplifies ROS production by inhibiting key antioxidant enzymes, thereby promoting the accumulation of destructive hydroxyl radicals (Fu and Xi, 2020; Thakur et al., 2025). A hallmark of Pb^{2+} toxicity is molecular mimicry of essential divalent cations, particularly calcium (Ca^{2+}) (Ettinger et al., 2007). Due to a similar ionic radius and charge, Pb^{2+} displaces Ca^{2+} from critical binding sites, disrupting neuronal signaling (Rădulescu and Lundgren, 2019), and substitutes for magnesium (Mg^{2+}) in enzymes such as pyrimidine 5'-nucleotidase, contributing to impaired erythropoiesis (Buc and Kaplan, 1978). Furthermore, Pb^{2+} directly targets mitochondrial integrity, disrupting the electron transport chain, ATP synthesis, and cytochrome c oxidase (Bandaru et al., 2022), which in turn exacerbates mitochondrial ROS formation and compromises cellular energy. The consequent oxidative stress inflicts direct DNA damage, while concurrently inhibiting DNA repair enzymes (*e.g.*, polymerases) (Hemmaphan and Bordeerat, 2022). Emerging evidence also points to Pb-induced epigenetic alterations (Mei et al., 2023) and immune dysregulation (Fenga et al., 2017), illustrating its broad, systems-level toxicity.

Chelation therapy is the primary treatment for heavy metal intoxication. An ideal chelator would selectively bind and eliminate the toxic metal from the body without adverse effects or depleting essential elements (Hoet et al., 2020). However, no current agent could achieve this (Kim et al., 2019). For instance, both sodium-calcium-ethylenediaminetetraacetic acid ($CaNa_2EDTA$) and succimer (DMSA) were used for lead chelation, but their use was limited by adverse effects. $CaNa_2EDTA$ can cause nephrotoxicity and non-selectively deplete essential ions such as zinc and copper. Although DMSA had a safer profile, it still increased the urinary excretion of these crucial elements (Sears, 2013). Beyond synthetic chelators, natural polymers—often referred to as phytochelators—are emerging as potential bioremediation agents for heavy metals. Complementary research explores the role of micronutrients, including vitamins, sulfur-containing amino acids, and essential minerals, in modifying the toxicokinetics and mitigating the adverse effects of metal ions (Sears, 2013). Sulfur-rich foods such as garlic (Abdalla et al., 2010) and broccoli (Bajguz, 2011) may enhance glutathione synthesis, supporting detoxification. In animal models, *Coriandrum sativum* reduced lead deposition in bone and inhibited δ-aminolevulinic acid dehydratase (ALAD) enzyme impairment (Aga et al., 2001).

The microalga *Chlorella* has gained attention both for its diverse metal-binding functional groups (*e.g.*, carboxyl, amino, phosphoryl) and its rich micronutrient profile, including vitamin B12, iron, and magnesium. Proposed detoxification mechanisms of *Chlorella* include direct chelation, antioxidant activity, and immunomodulation by polysaccharide components. *C. vulgaris* has a special bioactive component, *Chlorella* growth factor (CGF), which promoted the proliferation of Chinese hamster ovary (CHO) and mesenchymal stem cells (MSCs) in both 2D and 3D culture systems under low-serum conditions up to 21 days (Ng et al., 2020). However, the potential contribution of these proliferative effects to heavy metal detoxification processes remains unknown and warrants investigation. While human clinical evidence revealed the protective effects of algae on glucose and lipid homeostasis (Wu et al., 2023). A direct mechanistic link to heavy metal detoxification remains unestablished. Hence, elucidating the underlying modes of action of *Chlorella* is required to assess its therapeutic potential.

Cellular lead absorption and transport are accomplished through four primary mechanisms: albumin binding, divalent metal transporter 1 (DMT1), calcium channels, and P-type ATPases. Metallothioneins (MTs) play a crucial role in the intracellular binding of lead, rather than active transport proteins that move Pb^{2+} across cell membranes (Tripathi and Poluri, 2021). In this study, we focus on the role of transmembrane protein DMT1 in the *Chlorella* detoxification mechanism of lead. DMT1, also known as NRAMP2 or SLC11A2, mediates H^{+}-coupled transport of divalent metals (Fe^{2+}, Mn^{2+}, Cd^{2+}, Pb^{2+}) (Montalbetti et al., 2014). Diets rich in iron-containing foods could be protective against lead poisoning (Bannon et al., 2002), suggesting that lead tends to substitute for iron and disturb iron metabolism via a molecular mimicry mechanism. Beyond this, DMT1 is also expressed on astrocytes and brain endothelial cells, and Pb^{2+} particularly targets the developing brain in children (Sanders et al., 2009). Since the blood-brain barrier lacks significant endocytosis, lead transport into the brain likely occurs as either free Pb^{2+} or bound to small ligands, and DMT1 is a strong candidate for this transport. This mechanism is supported by evidence showing that elevated DMT1 expression increases lead transport into glial cells and explains why astrocytes accumulate Pb^{2+} *in vivo* (Bressler et al., 2004). In all, DMT1 is crucial in understanding cellular lead levels and susceptibility to lead toxicity.

In this study, we demonstrated that the aqueous extract of a commercial *C. vulgaris* supplement uniquely contains bioactive flavonoids (luteolin, apigenin), which were absent in the extracts of *C. pyrenoidosa*. This distinct metabolite profile established this aqueous extract of *C. vulgaris* as the superior candidate for subsequent investigation. The extract exhibited significant antioxidant capacity and may protect DMT1-overexpressing HEK-293 cells from Pb^{2+}-induced ferroptosis. Mechanistically, the extract facilitated the export of Pb^{2+}, potentially via the DMT1 transporter. This novel chelation activity may mitigate lead toxicity by attenuating the cellular iron-stress response. Specifically, it may reinstate autophagic flux, evidenced by the normalization of LC3-II and p62 protein levels, and may have triggered an adaptive metabolic shift via protein lipoylation by downregulating FDX1 and LIAS. The subsequent inhibition of dysregulated iron metabolism was further suggested by the recovery of NCOA4 and FTH1 expression, indicating a potential role in preventing Pb^{2+}-induced ferroptotic cell death. Furthermore, the extract's protective effect was critically

associated with modulation of p-STAT3 signaling and coincided with partial recovery of microtubule network polymerization. These findings demonstrate that *Chlorella* possesses substantial potential as a lead-chelating agent, with its detoxification efficacy closely linked to the regulation of iron homeostasis.

Materials and methods

Extraction of C. vulgaris and C. pyrenoidosa dietary supplements

Five grams of the *C. vulgaris* powder (Roquette Klötze GmbH & Co. KG, Germany) and *C. pyrenoidosa* powder (Sun Chlorella Corp., Kyoto, Japan) were extracted with a series of solvents: distilled water, MeOH: H_2O (7:3, v/v), and CH_2Cl_2: MeOH (1:1, v/v) by ultrasonication (2 h, 3 × 300 mL). Then, the extracts were filtered through Whatman filter paper and evaporated under vacuum until the dryness of solvents using a rotary evaporator at 40-50°C. The obtained crude extracts were expressed as a percentage of the dried biomass weight used (mg extract/g dry biomass weight). The dried extracts were stored at –20°C for UPLC-HRMS/MS as well as biological activity analyses. The stock solutions for the cytotoxicity studies were prepared at a concentration of 20 mg/mL by dissolving the extracts in distilled water or dimethyl sulfoxide (DMSO). Then, the required concentrations were prepared from the stock solution.

HPLC-HRMS/MS analysis

Dried extracts obtained from distilled water, MeOH: H_2O (7:3, v/v), or dichloromethane: methanol (1:1, v/v) preparations were reconstituted in their respective solvents to a final concentration of 1 mg/mL and subsequently diluted 1:1000. The resulting solutions were analyzed using a 1260 Infinity II high-performance liquid chromatography (HPLC) system (Agilent Technologies, Waldbronn, Germany) coupled to a 6545 QTOF mass spectrometer (Agilent Technologies) equipped with an Agilent Jet Stream electrospray ionization (ESI) source. Chromatographic separation was carried out on an Eclipse Plus C18 RRHD column (50 mm × 2.1 mm, 1.8 μm; Agilent Technologies) using a binary gradient of 2% acetonitrile in water (A) and methanol (B) as follows: 15% B for 1 min, linear increase to 95% B over 24 min, hold at 95% B for 5 min, return to 15% B within 1 min, and re-equilibrate at 15% B for 9 min using a flow rate of 0.2 mL/min; 5 μL. The mass spectrometric detection was performed in positive ion, automated data-dependent acquisition (DDA) mode, acquiring full MS scans (m/z 50–1500; 1 spectrum/s) followed by MS/MS scans of the two most intense ions, with active precursor exclusion after five spectra for 0.5 min. The ESI parameters were as follows: capillary voltage, 3.5 kV; nozzle voltage, 1.0 kV; fragmentor voltage, 175 (arbitrary units); drying gas temperature, 320°C; sheath gas temperature, 350°C; drying gas flow, 10 L/min; nebulizer pressure, 35 psig. High-purity nitrogen was employed as a nebulizing, auxiliary, and collision gas. Data were acquired in centroid mode, and the instrument was externally calibrated immediately before each sample set. The collision energy was fixed at 35 V. The dried extracts were prepared for UPLC-HRMS/MS analyses following a previously described protocol (Hegazi et al., 2020). The extracts (1 mg each) were dissolved in the mobile phase to a final concentration of 1 mg/mL and subsequently diluted 1:1000. The solutions were placed in an ultrasonic bath before injection and filtered through a 0.45 μm membrane filter.

Feature-based molecular networking and compound annotation

Two feature-based molecular networks (FBMNs) were constructed from the acquired UPLC-HRMS/MS data in both ionization modes. For data preprocessing, Mzmine 3.6.0 was used for feature detection, grouping, and alignment (Schmid et al., 2023). Initially, the MSConvert program was used to convert raw data files into 32-bit MzXML files, which were then loaded into Mzmine 3.6.0. The generated mgf files from the Mzmine were uploaded to the Global Natural Products Social Molecular Networking platform (https://gnps.ucsd.edu) to create two feature-based molecular networks (FBMNs) following the online protocol (Nothias et al., 2020). The parameters applied for the construction of the FBMNs via the GNPS platform are detailed in Supplementary Table S1. Cytoscape version 3.7.1.60 was used for the network visualization. Sirius + CSI: FingerID 5.6.3 was used for the manual putative structural identification, assisted by the molecular formula prediction and candidate search with m/z tolerance set to 20 ppm (Dührkop et al., 2019). The negative FBMN is available at: https://gnps.ucsd.edu/ProteoSAFe/status.jsp?task=cd9ef2b787394cca8d5bd7f0845652a1. The positive FBMN is available at: https://gnps.ucsd.edu/ProteoSAFe/status.jsp?task=a122ea45516c4670b8296f0a0b559d17.

Trolox equivalent antioxidant capacity (TEAC) assay

Antioxidant capacity of the extracts was evaluated by the improved $ABTS^{\cdot+}$ method, as described by Re et al. (Re et al., 1999) with slight modifications. Briefly, 2,2'-azinobis-(3-ethylbenzothiazoline-6-sulfonic acid) ($ABTS^{\cdot+}$) radical cation was generated by oxidation of ABTS with potassium persulfate and is reduced in the presence of antioxidants, resulting in decolorization, which can be detected in specific absorbance. First, 7 mM ABTS and 2.45 mM potassium persulfate were mixed overnight (12-16 h) in the dark at room temperature and were used within two days. The $ABTS^{\cdot+}$ solution was diluted with PBS to achieve an absorbance of around 0.700 at 415 nm. Different concentrations of extracts (0.0006-20 mg/mL) or Trolox (0-400 μmol) were mixed with diluted $ABTS^{\cdot+}$ solution in a ratio of 1:19. Trolox, the water-soluble α-tocopherol (vitamin E) analogue, served as a standard. The mixture was allowed to stand for 5 min at room temperature, and the absorbance was measured at 415 nm. Inhibition percentages of the extracts and Trolox in different concentrations were derived from absorbance measurements and analyzed using a linear regression model to determine the EC_{50} value of each. The results of the assay were expressed as μmol Trolox equivalent per gram of extract and calculated as the mean value ± standard deviation (SD) (n = 3).

Cytotoxicity determination

Human Embryonic Kidney 293 cells, HEK-293, and stably overexpressing pIRES2 DsRed-Express2-DMT1, HEK-293 DMT1 cell lines were cultured in DMEM supplemented with 10% FBS, 10 mM HEPES, 1 mM Na-pyruvate, and 100 μM minimal essential medium (MEM) nonessential amino acids at 37°C. *DMT1* encodes the divalent metal transporter 1. Additionally, the media used to culture the HEK-293 DMT1 cell line was also supplemented with 500 μg/mL geneticin (Sigma-Aldrich, Taufkirchen, Germany). Both HEK-293 and HEK-293 DMT1 cells were kindly provided by Prof. Matthias A. Hediger (University of Bern) (Montalbetti et al., 2014). DMT1 overexpression was verified in our laboratory by RT-qPCR (Supplement Fig. S1).

Cytotoxicity toward $Pb(NO_3)_2$ and *C. vulgaris* water extract was evaluated using the resazurin (Promega, Mannheim, Germany) reduction assay. The principle can be summarized as the living cells metabolically reduce the non-fluorescent dye resazurin into the highly fluorescent dye resorufin. $Pb(NO_3)_2$ was evaluated over a concentration gradient ranging from 0.003 μM to 100 μM, whereas *C. vulgaris* water extract was assessed over a concentration range of 0.003 μg/mL to 100 μg/mL. Additionally, a fixed concentration of 30 μg/mL *C. vulgaris* extract was applied to Pb^{2+}-exposed cells (0.003 μM to 100 μM) to evaluate its potential to restore cell viability. The fluorescence was measured after 72 h incubation with Infinite M2000 Pro™ plate reader (Tecan, Crailsheim, Germany) at an excitation wavelength of 544 nm and an emission wavelength of 590 nm. IC_{50} values were determined from concentration–response curves using linear regression analysis in Microsoft Excel and are presented as mean ± standard deviation (SD).

Each experiment was conducted independently three times, with six technical replicates per condition.

Intracellular and extracellular chelating effects: ICP-OES assay

The chelating potential of *C. vulgaris* water extract towards Pb^{2+} ions intracellular and extracellular of HEK-293 DMT1 cells was assessed over a time gradient (0.5 h, 2 h, 8 h, 24 h, 48 h, and 72 h). Aliquots of 5×10^4 cells/well were seeded in a 12-well plate and allowed to adhere overnight in 5% FBS-containing medium. Cells were subsequently treated with 1 μM of $Pb(NO_3)_2$, either alone or in combination with 30 μg/mL *C. vulgaris* water extract. EDTA-$CaNa_2$ (10 μM, Sigma-Aldrich), a clinical high-affinity lead chelator (Sidbury, 1955), served as a positive control. After each collection time point, the cell supernatant of each group was harvested and clarified by 0.22 μm PTFE membranes; To eliminate non-internalized surface-associated Pb^{2+}, cells were washed twice with ice-cold PBS supplemented with 0.5 mM EDTA. Afterwards, the cells were harvested by scraping and centrifugation and then counted for normalization. Sample digestion for ICP-OES analysis was carried out according to the sample pretreatment method developed by the Standard Methods Committee (Gabrelian et al., 2004) with slight modifications. Cell supernatant filtrates were digested with 700 μL of 65% nitric acid (Merck Millipore, Schwalbach, Germany), while cell pellets were digested using 400 μL of 65% nitric acid at 100 °C for 30 minutes, after which all samples were adjusted to 10 mL with ultrapure water (18.2 MΩ·cm). Pb^{2+} concentrations were then determined using ICP-OES. Calibration curves were generated using certified Pb standards (10 - 1000 ppb) prepared in 5% nitric acid. Intracellular metal concentrations were normalized to ng/cell, whereas extracellular concentrations were calculated directly in μg/L to quantify chelation efficiency. Each experiment was conducted independently in triplicate.

Detection of ferroptosis inhibition and cellular iron level

Ferroptosis inhibition in the samples was assessed using the resazurin reduction assay, following our established protocol (Mbaveng et al., 2019; Yan et al., 2020), and the 2025 'Expert Recommendation' on ferroptosis authored by Prof. Marcus Conrad (Mishima et al., 2025), with minor modifications. A total of 5000 cells per well were seeded in a 96-well plate and incubated for 24 h in medium containing 5% FBS to allow for cell attachment. Then, the cells were pre-treated with 0.5 μM iron chelator deferoxamine (Sigma-Aldrich, Taufkirchen, Germany) for 2 h at 37°C. Subsequently, the cells were exposed to stepwise increasing concentrations of $Pb(NO_3)_2$, ranging from 0.003 μM to 100 μM, for 72 h without deferoxamine removal. Cell viability was assessed as previously described using the resazurin reduction assay. Data were derived from three independent experiments, each conducted with six technical replicates, and are presented as 50% inhibition concentration (IC_{50}) values.

The intracellular ferrous iron (Fe^{2+}) levels were determined using the Cell Ferrous Iron Colorimetric Assay Kit (E-BC-K881-M, Elabscience, Wuhan, China). Cells were treated with 0.3 μM of lead nitrate ($Pb(NO_3)_2$, Sigma-Aldrich), either alone or combined with 30 μg/mL *C. vulgaris* water extract. Untreated cells served as a negative control. 0.5 μM iron chelator deferoxamine (DFO) served as a positive control. The 593 nm absorbance values were used to quantify the intracellular Fe^{2+} levels by reference to a standard calibration curve.

Gene expression profiles

Total mRNA was isolated using the InviTrap® Spin Universal RNA Mini Kit (Invitek Molecular, Berlin, Germany), and the total RNA concentrations were determined using the NanoDrop1000 Spectrophotometer (PEQLAB, Erlangen, Germany). HEK-293 and HEK-293 DMT1 cells (1×10^6 cells/well) were used as controls, and cells were treated with $Pb(NO_3)_2$ only (0.3 μM) or *C. vulgaris* water extract (30 μg/mL) together for 24 h in duplicate. The concentrations of $Pb(NO_3)_2$ and *C. vulgaris* water extract were selected according to the maximum recovery of cell viability observed in Pb^{2+}-exposed HEK-293 DMT1 cells following treatment with *C. vulgaris*. Afterwards, quality control of total RNA, probe labeling, hybridization, scanning, and data analysis of the samples were performed at the Genomics and Proteomics Core Facility of the German Cancer Research Center (DKFZ, Heidelberg, Germany). Affymetrix GeneChips® with human Clariom™ S assays (Affymetrix, Santa Clara, CA, USA) were applied for microarray hybridizations as previously described in detail (Hegazy et al., 2021). Venn diagrams were generated by software at the website http://bioinformatics.psb.ugent.be/webtools/Venn/

Ingenuity pathway analysis (IPA)

Microarray hybridization data were analyzed using the Chipster data analysis platform (CSC, Espoo, Finland) to identify high-confidence transcriptional changes. The workflow included filtering genes by coefficient of variation (0.1) and identifying significantly differentially expressed genes (DEGs) using the empirical Bayes moderated t-test. The resulting *p*-values were then subjected to multiple testing correction via the Benjamini-Hochberg method to control the false discovery rate (FDR-adjusted $p < 0.1$). This curated list of DEGs was fed into Ingenuity Pathway Analysis (IPA) software (Ingenuity Systems, Redwood City, CA, USA) to infer the impact of treatment on cellular pathways and biological functions (Thomas and Bonchev, 2010). The significance and predicted states of pathways and biological functions in IPA were determined by integrating two statistical measures: *p*-value and activation Z-score. Enrichment significance *p*-value was calculated using Fisher's exact test without taking into account the regulation direction, which assesses the probability that the overlap between the submitted gene list and a pre-defined pathway occurs by chance in the Ingenuity Knowledge Base. Z-score was defined to predict the directional perturbation ($Z>0$ activation or $Z<0$ inhibition) and significance ($|Z|>2$) of pathways. This Z-score algorithm quantitatively evaluates the consistency between the observed up- and down-regulation patterns of genes within a pathway and the causally annotated relationships stored in Ingenuity Knowledge Base, thereby enabling the identification of functionally relevant signaling pathways perturbed by the treatment conditions (Krämer et al., 2014).

Validation of gene expression by quantitative real-time reverse transcription PCR (qRT-PCR)

To validate the chip results, the expression of eight genes of interest that were associated with the enriched canonical pathways was analyzed with qRT-PCR. The same total RNA samples (control Pb^{2+} exposure and co-treatment of *C. vulgaris* water extract with Pb^{2+}) used for the microarray analyses were also used for qRT-PCR experiments. An aliquot of 1 μg of total RNA was reverse transcribed to cDNA using the LunaScript® RT SuperMix Kit (New England Bio Labs, Darmstadt, Germany) according to the manufacturer's instructions. Gene-specific primers were designed using the NCBI Primer-BLAST website (https://www.ncbi.nlm.nih.gov/tools/primer-blast/), and all primers were synthesized by Eurofins Genomics (Ebersberg, Germany). *GAPDH* served as an internal gene for normalization. The cycle quantification (Cq) values were determined using CFX Manager Software (version 3.1). The relative gene expression was calculated using the comparative $2^{-\Delta\Delta CT}$ method (Livak and Schmittgen, 2001).

Assessment of ferroptosis, autophagy, apoptosis, protein lipoylation, and cellular growth factors by western blotting

HEK-293 and HEK-293 DMT1 cells were treated with $Pb(NO_3)_2$ alone (0.3 μM) or in combination with *C. vulgaris* water extract (30 μg/mL) for 72 h. Untreated HEK-293 DMT1 cells served as a control. Cytoplasmic and nuclear proteins were extracted from harvested cells using M-PER®

Mammalian Protein Extraction Reagent supplemented with EDTA-Free Halt Protease and Phosphatase Inhibitor Cocktail (Thermo Scientific, Darmstadt, Germany) according to the manufacturer's instructions. Afterwards, protein lysates (20 μg per sample) were denatured at 95°C for 10 min and separated by sodium dodecyl sulfate polyacrylamide gel electrophoresis (SDS-PAGE). Separated proteins were transferred to a polyvinylidene fluoride (PVDF) membrane (Carl Roth, Karlsruhe, Germany). Membranes were washed several times with Tris-buffered saline containing 0.5% Tween-20 (TBST), then blocked with 5% (w/v) bovine serum albumin in TBST for 1 h at room temperature. Subsequently, membranes were incubated at cold room overnight with primary antibodies, including NCOA4 (1:1000, Cell Signaling Technology, Frankfurt a. M., Germany), FTH1 (1:1000, Cell Signaling Technology), Beclin-1 (1:1000, Cell Signaling Technology), LC3B (Microtubule-associated proteins 1A/1B light chain 3 β, 1:1000, Cell Signaling Technology), p62 (1:1000, Proteintech, Planegg-Martinsried, Germany), PARP, Caspase-3 and Bcl-xL (1:1000, Cell Signaling Technology), DLAT (1:1000, Cell Signaling Technology), FDX1 (1:1000, Proteintech), LIAS (1:3000, Proteintech), PI3K and Phospho-PI3K (1:1000, Cell Signaling Technology), STAT3 and Phospho-STAT3 (1:1000, Cell Signaling Technology), GAPDH (1:1000, Cell Signaling Technology) and β-actin (1:1000, Cell Signaling Technology). Following the three washes with TBST, membranes were incubated with horseradish peroxidase-linked IgG secondary antibodies (1:2000 or 1:4000, Cell Signaling Technology) at room temperature. After subsequent TBST washes, immunoreactive bands were detected using Luminata™ Classico Western HRP substrate (Merck Millipore) and visualized with an Alpha Innotech FluorChem Q system (Biozym, Oldendorf, Germany).

Fluorescence microscopy of the microtubule cytoskeleton

HEK-293 DMT1 cells were seeded in μ-Slide 8 Well chambers (5×10^4 cells/well, ibidi, Gräfelfing, Germany) and allowed to adhere overnight at 37°C in the incubator with 5% CO_2. Cells were then exposed to 0.3 μM $Pb(NO_3)_2$ alone or co-treated with 30 μg/mL *C. vulgaris* water extract. Untreated HEK-293 DMT1 cells served as a negative control, while 20 nM vincristine was applied as a positive control. After 24 h treatment, cells were washed with PBS, then fixed with ice-cold 4% paraformaldehyde (PFA) at -20°C for 10 min. The samples were subsequently permeabilized and blocked in PBS containing Triton™ X-100 (Sigma-Aldrich) for 1 h at room temperature. Microtubules were labeled by a β-tubulin primary antibody (1:100, Cell Signaling Technology) overnight at 4°C. The following day, cells were washed with PBS and incubated with anti-rabbit IgG (H+L), $F(ab')_2$ secondary antibody (1:2000, Cell Signaling Technology) for 1 h at room temperature. Nuclei were counterstained with Hoechst 33342 Nuclear Stain (BioVision, Wiesbaden, Germany) for 5 min at room temperature in the dark. Excessive Hoechst stain was removed by washing with PBS, and cells were mounted with ibidi mounting medium (Ibidi). The fluorescence imaging was performed using an AF7000 widefield microscope (Leica Microsystems, Wetzlar, Germany). GFP was detected at 488 nm excitation and 527 nm emission. Hoechst stain was detected at 432 nm excitation and 470 nm emission. Images were captured using Fiji ImageJ software.

Statistics

Statistical analyses were performed using GraphPad Prism software (version 10). Data are presented as the mean ± standard deviation (SD) from three independent biological replicates. One-way or two-way analysis of variance (ANOVA) was performed, followed by Tukey's post hoc test. Statistical significance is denoted as follows: not significant (ns), $*p < 0.05$, $**p < 0.01$, and $***p < 0.001$.

Results

UPLC-HRMS/MS metabolite profiling of the extracts

The first objective of our study was to characterize and compare the secondary metabolic profiles of two different *Chlorella* species. For this purpose, we analyzed two widely utilized, commercially available Chlorella supplements: *C. vulgaris* (*CV*) and *C. pyrenoidosa* (*CP-J*) and extracted them with three different solvents (i.e., dichloromethane: MeOH (1:1, v/v), 70% MeOH, and H_2O). Untargeted metabolomics using UPLC-HRMS/MS in both ionization modes was recruited for this purpose. The base peak chromatograms in both ionization modes showed quite different metabolomic profiles of the studied *Chlorella* species when extracted with different solvents (Fig. 1).

For a comprehensive view of the underlying similarities and differences among the studied *Chlorella* species, FBMNs were constructed (Fig. 2). The positive FBMN comprised 665 nodes with 296 connected features across 45 clusters, and the remaining nodes were singletons (Fig. 2A). The negative FBMN included 802 features, with 451 grouped nodes across 34 clusters, and the remaining features were singletons (Fig. 2B). The FBMNs revealed the prevalence of several lipid classes, mainly glycerolipids and phospholipids (Fig. 2, Supplementary Table S1). Additionally, the negative FBMN allowed for the detection of a cluster of a few benzoic acid derivatives and some flavonoids observed as singletons, especially in *C. vulgaris* extracts (Fig. 2B, Supplementary Table S1). The detected pigments were mainly porphyrins, found exclusively in the positive FBMN (Fig. 2A). As evident from the BPCs and the constructed FBMNs, *C. vulgaris* exhibited a richer secondary metabolomic profile and higher diversity of metabolites.

The detailed fragmentation and ion mode of each annotated feature are listed in Supplementary Table S1. The following section provides a detailed discussion of the annotated metabolite classes, presented in elution order.

Benzoic acids

A couple of benzoic acid derivatives were grouped in a small cluster in the negative FBMN. These occurred in both species (Fig. 2B) and were identified as isomers of hydroxybenzaldehyde (2–4) and hydroxybenzoic acid methyl ester (5) (Supplementary Table S1).

Flavonoids

In addition to being valued for their prolific lipid production, microalgal species have been recently shown to biosynthesize flavonoids simultaneously (Yadavalli et al., 2020). During our analysis, we identified several common and valuable flavonoids that occurred uniquely in *C. vulgaris* extracts and annotated them as luteolin-O-hexoside (6), tetrahydroxymethoxyflavone (7), luteolin (8), apigenin (10), which bear a flavone core, and methyl quercetin (9) in the flavonol structure (Supplementary Table S1).

Lipids

Further, the constructed FBMNs shed light on the lipid classes abundantly present in the studied *Chlorella* species, indicating their potential value as nutrient and biodiesel candidates. Replicated lipids were commonly substituted with fatty acids with C14-C18 chains and 2-3 degrees of unsaturation, as per previous studies (Pantami et al., 2020). The visual inspection of the FBMNs revealed lipid classes, including glycolipids, phospholipids, and free fatty acids (Fig. 2). Different classes of glycerolipids were noticed in the examined Chlorella samples extracted with 70% MeOH and dichloromethane: methanol (1:1), including diglycosidic monacyl glycerols (DGMG) and monoglycosidic monoacyl glycerols (MGMG) along with tri-, di-, and mono-acyl glycerols (TG, DG, and MG), substituted with polyunsaturated fatty acids

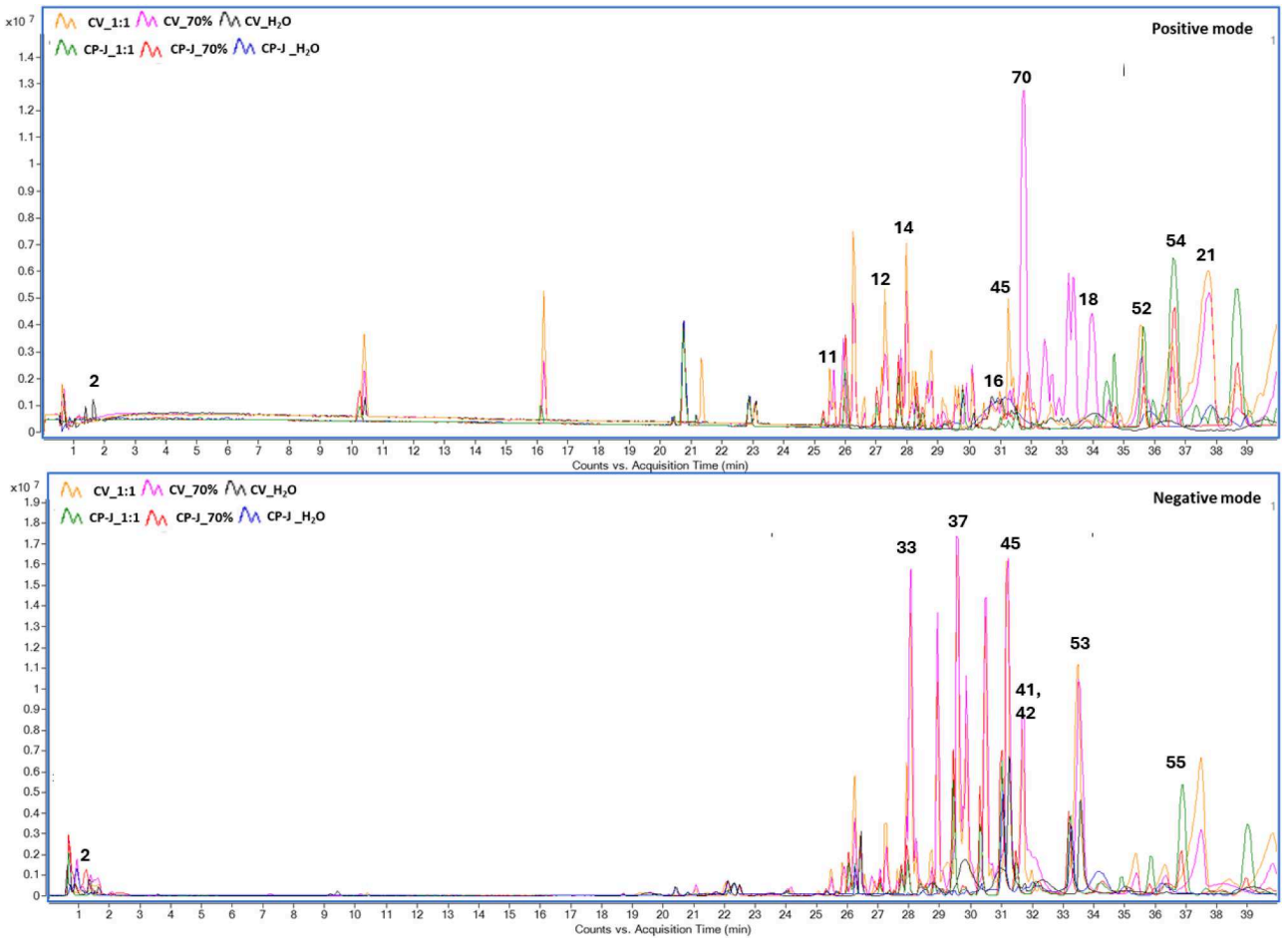


Fig. 1. The base peak chromatograms (BPC) of *C. vulgaris* (CV) and *C. pyrenoidosa* (CP-J) extracted with three different solvents as analyzed by UPLC-HRMS-MS using both ionization modes.

(Supplementary Table S1). They were chiefly spotted in the positive FBMN, both as [M+Na]+ and sometimes as [M+H]+ adducts, with the glycosidic derivatives showing a fragmentation sequence of loss of a hexose moiety (-162 Da), two hexoses (-324 Da), and the fatty acyl group as (-RCOOH) (Melo et al., 2015). Annotated diglycosidic monoacyl glycerolipids (DGMG) included DGMG (16:3) (11), DGMG (18:3) (12), DGMG (16:1) (13), and DGMG (16:0) (15). Similarly diacyl glycolipids (MGDG) were observed such as MGDG(18:3/18:3) (16, 18 and 24), MGDG(18:2/18:2) (19), MGDG(18:2/18:3) (21), MGDG (18:2/16:3) (22), MGDG(16:2/16:2) (23), MGDG(18:3/18:3) (24), GDG (16:4/18:3) (25), MGDG(16:3/16:2) (26), MGDG(16:3/18:3) (27) (Supplementary Table S1). Lastly, acylglycerols were found, including the monoacyl glycerol; MG (18:3) (14), the diacyl glycerol; DG (14:1/18:2) (17), and the triacyl glycerols; TG (8:0/8:0/8:0) (20) and TG (10:0/8:0/8:0) (28) (Supplementary Table S1).

Chlorella species are known to produce various classes of phospholipids, such as phosphatidylcholines (PCs), phosphatidylethanolamines (PEs), and phosphatidylglycerols (PGs) (Hegazi et al., 2024). These phospholipids are not only essential components of cell membranes but also aid in the transport of materials across them. Besides, nutraceutically valued phospholipids are rich in polyunsaturated fatty acids and are used in the pharmaceutical and cosmetic industries (Maciel et al., 2016). The constructed FBMNs identified four classes of phospholipids in *Chlorella* samples extracted with both 70% MeOH and dichloromethane: methanol (1:1), namely PCs, phosphatidylinositols (PIs), PEs, and PGs. Phosphatidylcholines were better observed in the positive ionization mode and were distinguished by fragment ions at m/z 184 and 104, respectively, for the phosphocholine and choline moieties (Hegazi et al., 2021). Other phospholipids were observed in negative ionization mode and showed loss of their respective acyl moieties. Detected phospholipids were substituted with acyl chains of C16-C18 chains with 2-3 degrees of unsaturation (Supplementary Table S1).

Porphyrins

The characteristic green color of the *Chlorella* species is attributed to the porphyrins (*i.e.*, chlorophyll pigments) and carotenoids. However, only porphyrins were detected in the positive FBMN, exclusively in *C. vulgaris* extracts (Fig. 2, Supplementary Table S1). Their fragmentation pattern showed losses of H_2O, CO, and CH_2, consistent with their substitutional pattern as previously reported (Mishra et al., 2014; Rosell-Melé et al., 1999). The detected porphyrins include bacteriochlorin a (70), purpurin dimethyl ester (71), isomers of harderoporphyrin (72-74), phaeophorbide B, methyl ester (76), isomers of pheophorbide a (77 and 78), methyl pheophorbide a (79), phylloerythrin (80), and others (Supplementary Table S1). In addition to the previously discussed abundant metabolites, free fatty acids and fatty amides were also observed, as tabulated in Supplementary Table S1.

Trolox equivalent antioxidant capacity (TEAC) and cytotoxicity of C. vulgaris extracts

Following the chemical characterization, the antioxidant capacities of four different *C. vulgaris* extracts were measured by the TEAC assay. For further experimentation, we focused on *C. vulgaris* as this species uniquely contains flavonoids (luteolin, apigenin) and chlorophyll-

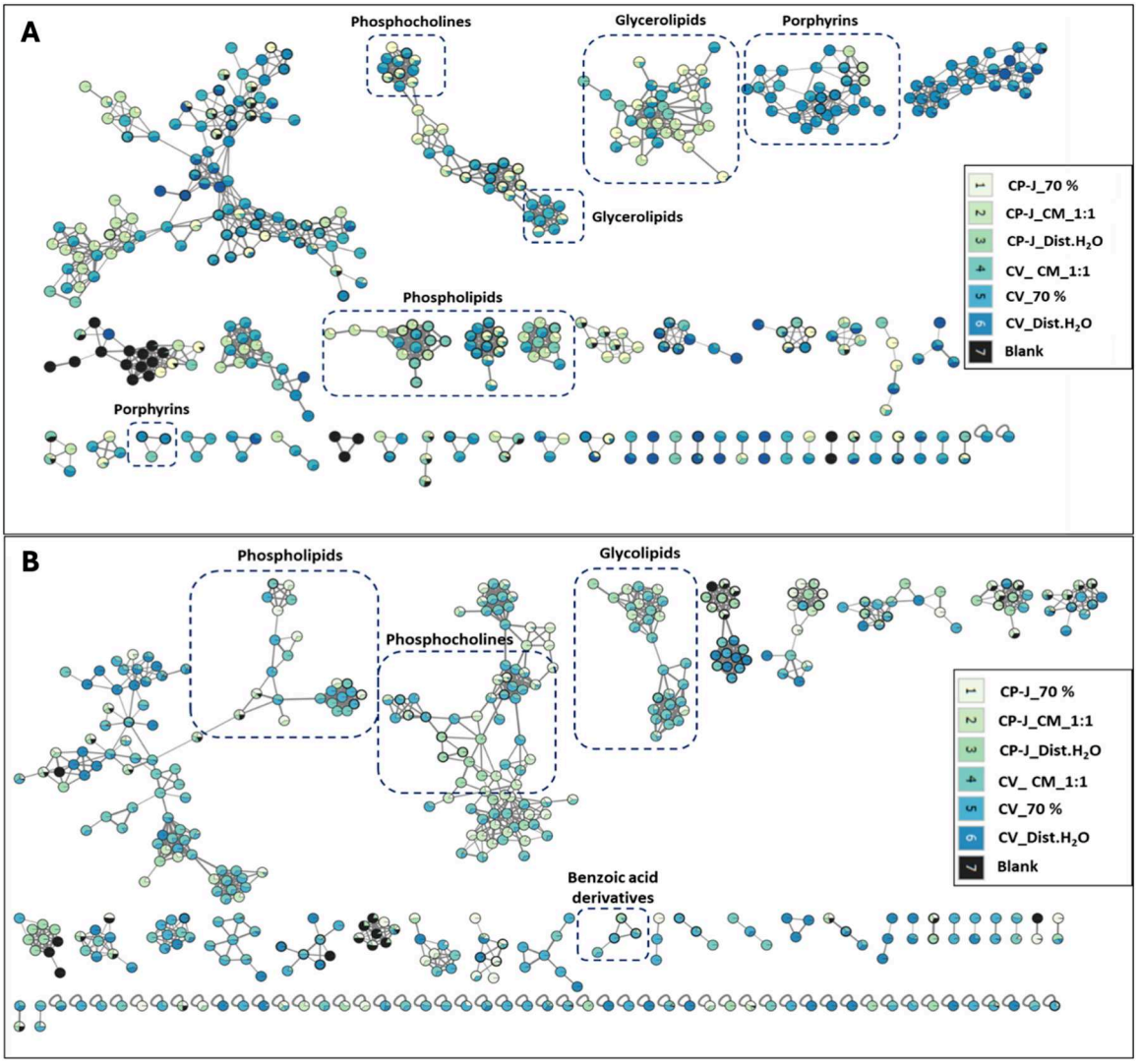


Fig. 2. Feature-based molecular network (FBMN) of acquired UPLC-HRMS/MS data in (A) positive ionization mode and (B) negative ionization mode of *Chlorella* samples using different extraction solvents.

derived porphyrins were detected exclusively in its extracts compared with *C. pyrenoidosa*. Notably, the antioxidant capacity of the *C. vulgaris* extracts were ranked as distilled water > dichloromethane: methanol (1:1) > hexane > MeOH: H_2O (7:3), with the highest value of 54.72 μmol Trolox eq/g in the distilled water extract (Fig. 3A). As *C. vulgaris* distilled water extract has the highest antioxidant capacity, the cytotoxicity of distilled water extract was tested in the HEK-293 and HEK-293 DMT1 cell lines. At all concentrations tested, the *C. vulgaris* distilled-water extract did not adversely affect the viability of either cell line (Fig. 3B).

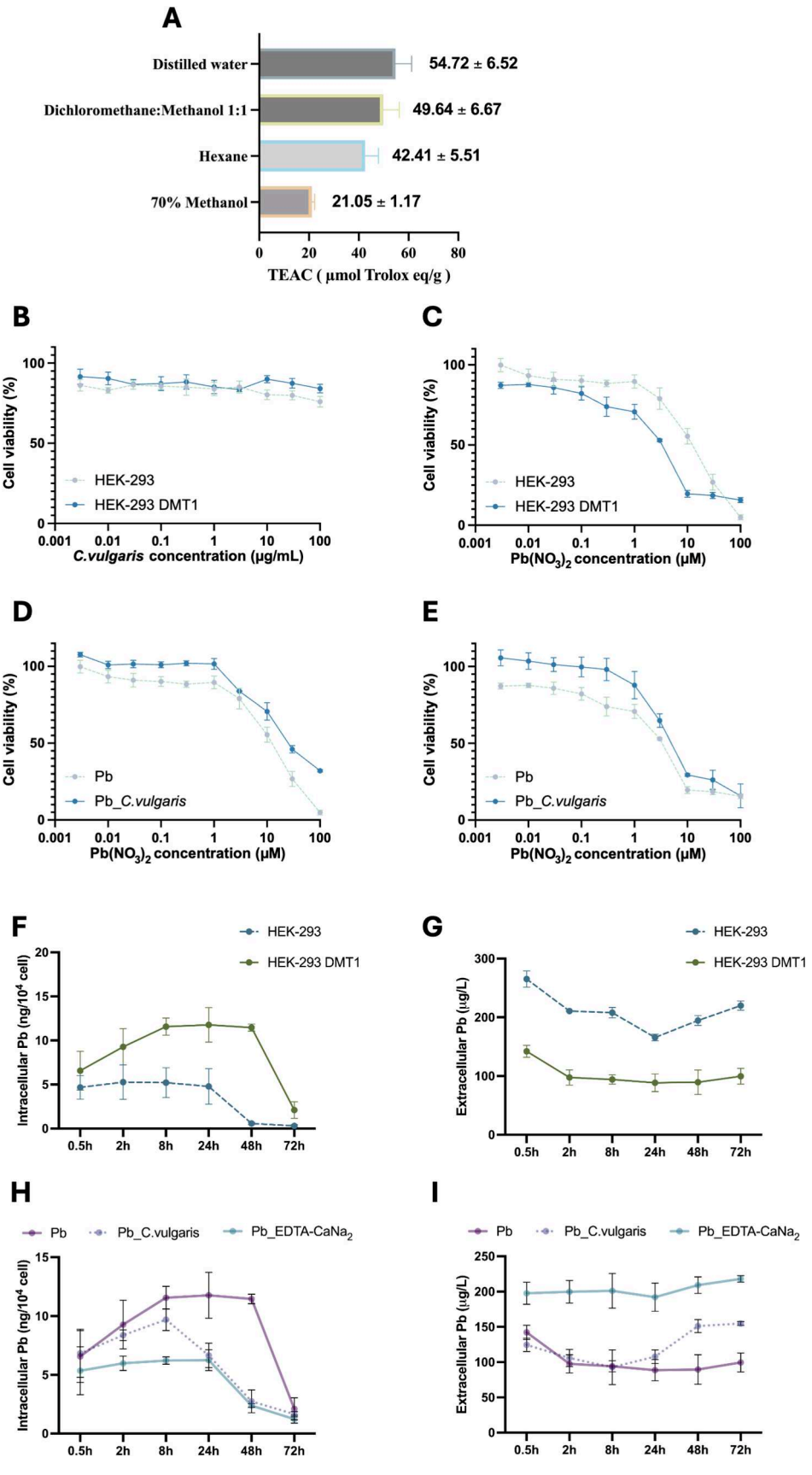
Lead uptake is facilitated by the divalent metal transporter 1 (DMT1)

The cytotoxicity of $Pb(NO_3)_2$ towards HEK-293 cells and HEK-293 DMT1 cell lines was examined because DMT1 confers lead transport (Bressler et al., 2004). Consistent with the previous literature, $Pb(NO_3)_2$ showed high sensitivity towards HEK-293 DMT1 cell line with a 4.01-fold change of IC_{50} value compared to wild-type cells (Table 1, Fig. 3C). The intracellular and extracellular concentrations of Pb^{2+} were also quantified by ICP-OES at 0.5 h, 2 h, 8 h, 24 h, 48 h, and 72 h. In HEK-293 cells, intracellular Pb^{2+}concentrations gradually increased from 0.5 h to 24 h, whereas extracellular Pb^{2+} concentrations showed a corresponding decrease (Fig. 3F and G). A similar trend was observed in HEK-293 DMT1 cells, with a more pronounced increase in intracellular Pb^{2+} from 0.5 h to 48 h at correspondingly decreased extracellular Pb^{2+} concentrations (Fig. 3F and G). Notably, intracellular Pb^{2+} concentrations from 8 h to 48 h were significantly higher in HEK-293 DMT1 cells compared with HEK-293 cells (Fig. 3F), accompanied by significantly lower extracellular Pb^{2+} concentrations at the same time point (Fig. 3G).

C. vulgaris chelation of lead enhances cell viability

A fixed concentration of 30 μg/mL *C. vulgaris* water extract was applied to Pb^{2+}-exposed cells (0.003 μM to 100 μM) to evaluate its potential to restore cell viability. At a concentration of 0.3 μM Pb^{2+}, *C. vulgaris* water extract showed maximum restored cell viability in the HEK-293 DMT1 cell line, with a value of 24.11% from 73.94% to 98.05%, corresponding to 13.57% from 88.42% to 101.98% in the wild-type cell line. Meanwhile, in the presence of *C. vulgaris* water extract, the cytotoxicity of Pb^{2+} decreased to 1.8- and 1.6-fold change, respectively (Fig. 3D and E, Table 1).

Based on the higher Pb^{2+} accumulation observed in HEK-293 DMT1 cells compared with HEK-293 cells (Fig. 3F and G), subsequent experiments assessing the chelating effect of *C. vulgaris* water extract were conducted exclusively in HEK-293 DMT1 cells by ICP-OES. The well-known metal chelator EDTA-$CaNa_2$ was used as a positive control and exhibited a strong chelation effect, reflected by consistently high



(caption on next page)

Fig. 3. The protective chelation of Pb^{2+} by *C. vulgaris* water extract improves cell viability (A-I). (A) Trolox equivalent antioxidant capacity of *C. vulgaris* distilled water, MeOH: H_2O (7:3), hexane, and dichloromethane: methanol (1:1) mixture extract. (B-C) The dose-response curves of *C. vulgaris* aqueous extract and $Pb(NO_3)_2$ towards HEK-293 and HEK-293 DMT1 cell lines. Cell viability of $Pb(NO_3)_2$-exposed and *C. vulgaris* water extract-treated plus $Pb(NO_3)_2$-exposed (D) HEK-293 and (E) HEK-293 DMT1 cell lines. (F) Intracellular and (G) extracellular concentrations of Pb^{2+} in HEK-293 and HEK-293 DMT1 cell lines from 0.5 h to 72 h. (H) Intracellular and (I) extracellular concentrations of Pb^{2+} by *C. vulgaris* aqueous extract or EDTA-$CaNa_2$ treatment in the Pb^{2+}-exposed HEK-293 DMT1 cell line from 0.5 h to 72 h. Data (A-E) are mean ± SD from n = 3 independent experiments, data (F-I) are mean ± SEM from n = 4 independent experiments.

Table 1
Cytotoxicity of *C. vulgaris* water extract, Pb^{2+}, and co-treatment with both agents towards HEK-293 and HEK-293 DMT1 cell lines.

Treatment	IC_{50} of HEK-293 (μM)	IC_{50} of HEK-293 DMT1 (μM)
C. vulgaris	-	-
$Pb(NO_3)_2$	14.49 ± 2.23	3.61 ± 0.15
Pb^{2+} plus *C. vulgaris*	26.58 ± 2.50	5.89 ± 0.57
Pb^{2+} plus deferoxamine	70.56 ± 2.41	9.18 ± 0.87

extracellular Pb^{2+} concentration across all time points (Fig. 3I). Compared with Pb^{2+}, treated with *C. vulgaris* water extract showed a reduced rate of intracellular Pb^{2+} concentration from 0.5 to 8 h, followed by a progressive decrease from 8 to 72 h, indicating the promoted Pb^{2+} efflux contributed more significantly than reduced influx (Fig. 3H). Notably, the decrease of intracellular Pb^{2+} from 24 to 72 h closely paralleled the trend observed with EDTA-$CaNa_2$ (Fig. 3H). Correspondingly, extracellular Pb^{2+} concentration displayed the opposite pattern in the *C. vulgaris* water extract group, although the magnitude of the increase was less pronounced than that observed with EDTA-$CaNa_2$ (Fig. 3I).

Effects of $Pb^{2+}$and C. vulgaris treatment on microarray gene expression profiles

To investigate the potential mode of action of $Pb(NO_3)_2$ and the recovery mode of action of *C. vulgaris* extract on HEK-293 cells and HEK-293 DMT1 cells, gene expression analysis was done by microarray hybridization and IPA. Significantly deregulated genes were identified and compared to untreated controls using empirical Bayes with the FDR-corrected *p*-value < 0.1 by Benjamini-Hochberg (BH) and $|\log_2$ fold change$|$ > 0.6. Poisoning of $Pb(NO_3)_2$ in HEK-293 cells and HEK-293 DMT1 cells deregulated the expression of 226 and 246 genes, respectively. After the recovery with *C. vulgaris* water extract, the number of deregulated genes decreased to 154 and 130 genes in HEK-293 cells and HEK-293 DMT1 cells, respectively. $Pb(NO_3)_2$ and Pb^{2+} plus *C. vulgaris* shared 34 and 29 deregulated genes in HEK-293 cells and HEK-293 DMT1 cells, respectively (Fig. 4A and B).

For technical verification eight selected genes (*PHC3, ZNF217, XRCC5, TOR2A, ARID3B, TASOR2, ANAPC4*, and *ZNF205*) were quantified using qRT-PCR to validate the microarray hybridization results in both cell lines (Fig. 4E). Total mRNA was isolated from HEK-293 cells and HEK-293 DMT1 cells following 24 h treatment with 0.3 μM $Pb(NO_3)_2$ or 0.3 μM $Pb(NO_3)_2$ supplemented with 30 μg/mL *C. vulgaris* water extract, before performing microarray hybridization. The top eight upregulated and downregulated genes in the microarray data of HEK-293 and HEK-293 DMT1 cells showed consistent results in qRT-PCR. The correlation coefficient (r^2) between mRNA expression values measured by microarray and qRT-PCR was 0.90 and 0.91 in HEK-293 and HEK-293 DMT1 cells, respectively, indicating a high correlation between the two methods (Fig. 4E).

Effects of Pb^{2+} on "toxicity" or "diseases and functions" as predicted by IPA

Toxicity was one of the main issues we were concerned about: As a consequence, the toxicity was predicted in Pb^{2+}-exposed HEK-293 cells and HEK-293 DMT1 cells by IPA. In HEK-293 cells, IPA predicted that Pb^{2+} poisoning was mainly related to cardiac, liver and renal toxicity by the significant predictions (–log *p*-value > 1.3) of cardiac arrhythmia, cardiac arteriopathy, cardiac congestive cardiac failure, cardiac enlargement and heart failure, hepatocellular carcinoma, liver damage and liver hyperplasia, nephrosis, pulmonary hypertension and renal damage (Fig. 4C). In DMT1-overexpressing cells, Pb^{2+} poisoning shifted to liver and renal toxicity with the significant prediction of hepatocellular carcinoma, liver damage, liver hyperbilirubinemia, liver hyperplasia, nephrosis, renal damage, renal dysplasia, renal hypoplasia, renal inflammation, and renal nephritis (Fig. 4D).

Meanwhile, in "Diseases and cellular functions" predicted by IPA, Pb^{2+} significantly affected more or less the same diseases and functions as shown in the bar length by the -log *p*-value between HEK-293 cells and HEK-293 DMT1 cells (Fig. 4F to I). Notably, post-translational modification and molecular transport were significantly linked to Pb^{2+}-affected cellular function (Fig. 4F and G). "Organismal injury and abnormalities" and "Endocrine system disorders" were the most significant predicted Pb^{2+}-induced diseases in HEK-293 cells (Fig. 4H and I).

Comparison of canonical pathways as predicted by IPA

We found some clues of *C. vulgaris* ameliorative effect in Pb^{2+}-exposed HEK-293 and HEK-293 DMT1 cells by comparing canonical pathways in IPA prediction. Remarkably, the "Generic transcription pathway" was significantly activated in Pb^{2+}-exposed HEK-293 cells but was inhibited upon *C. vulgaris* treatment. Furthermore, this activation in Pb^{2+}-exposed cells and the subsequent inhibition upon *C. vulgaris* treatment were more pronounced in HEK-293 DMT1 cells (Fig. 5A). Then, we studied the genes involved in this pathway and discovered a striking pattern: 15 out of 16 genes, virtually the entire set, were zinc finger genes (Fig. 5B).

In HEK-293 cells, notably, all canonical pathway disorders predicted by IPA in Pb^{2+}-exposed HEK-293 cells ($|Z|>0$) were completely rescued by *C. vulgaris* treatment (Fig. 5D), with all affected pathways returning to a neutral state (Z-score = 0 or N/A). Meanwhile, these pathways exhibited opposite significance of -log *p*-value in Pb^{2+}-exposed HEK-293 cells compared to the *C. vulgaris* treatment group (Fig. 5C). In HEK-293 DMT1 cells, Pb^{2+}-exposed cells exhibited significantly enriched autophagy and ferroptosis-related pathways (-log *p*-value > 1.3), including the CLEAR signaling pathway, mTOR pathway, microautophagy signaling pathway, iron uptake and transport, iron homeostasis, and ferroptosis signaling pathway (Fig. 5E, Table 2). Importantly, all of these pathways decreased to a non-significant level (–log *p*-value < 1.3) following *C. vulgaris* treatment (Fig. 5E, Table 2), indicating a strong ameliorative effect. Meanwhile, Pb^{2+} exposure was predicted to activate the mTOR signaling pathway and inhibit the microautophagy signaling pathway in HEK-293 DMT1 cells (Fig. 5F). Notably, these predicted activation and inhibition patterns were no longer observed following *C. vulgaris* treatment (Fig. 5F). Moreover, protein lipoylation, a critical metabolic nexus linking autophagy and ferroptosis, also emerged as relevant. IPA predicted that the "Lipoate biosynthesis and incorporation II" remained significantly enriched –log *p*-value in both Pb^{2+}-exposed and *C. vulgaris* -treated HEK-293 DMT1 cells (Fig. 5E, Table 2).

Given these findings, subsequent analyses will focus on autophagy, ferroptosis, and protein lipoylation mechanisms in HEK-293 DMT1 cells, since IPA predicted these pathways as key points of divergence between the Pb^{2+}-exposed and *C. vulgaris* treatment group.

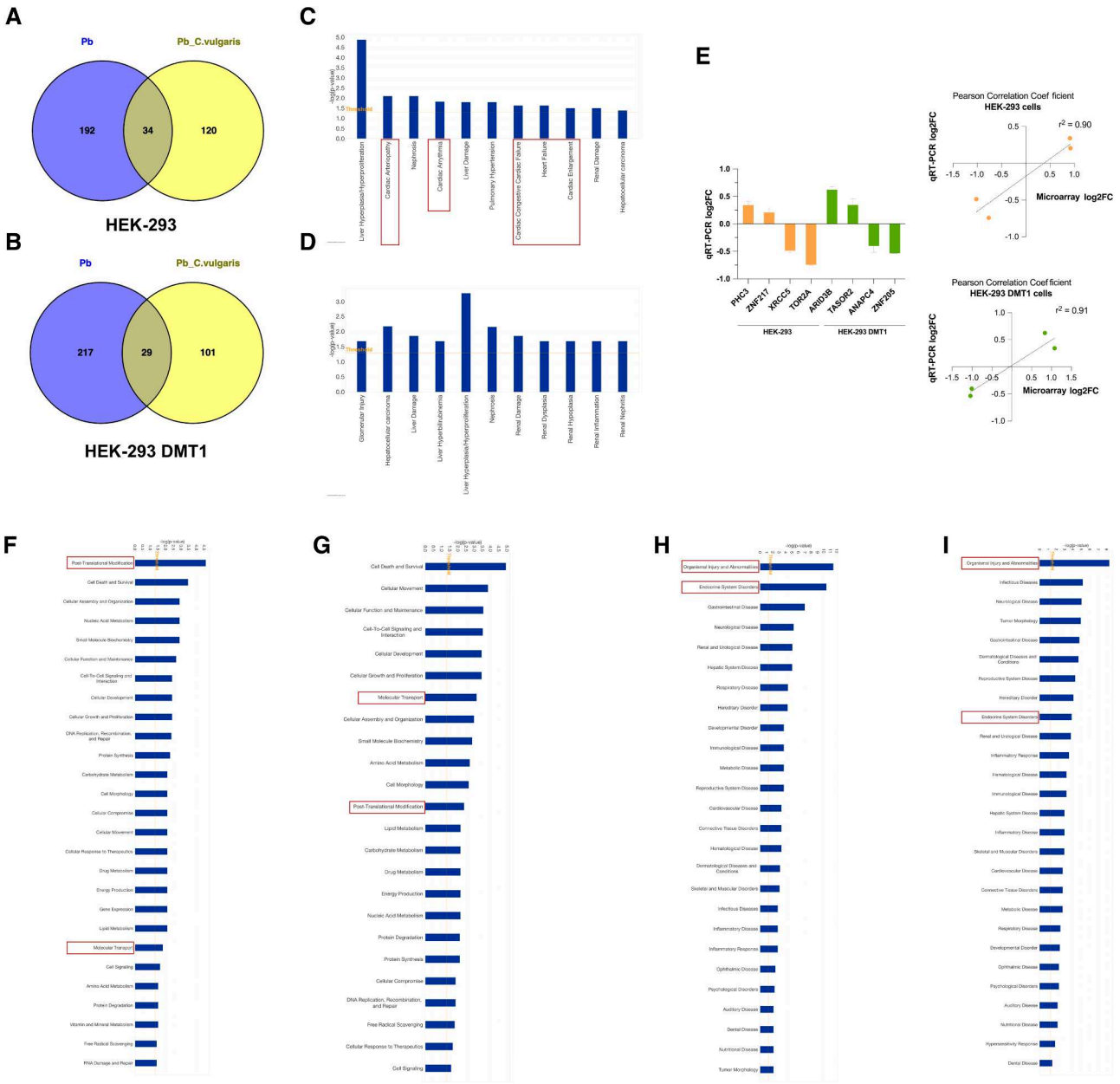


Fig. 4. Venn diagrams of deregulated gene expression upon treatment with 0.3 μM of Pb^{2+} and co-treatment with 30 μg/mL *C. vulgaris* aqueous extract in (A) HEK-293 cells and (B) HEK-293 DMT1 cells. IPA predicted toxicity in (C) Pb^{2+}-exposed HEK-293 cells and (D) HEK-293 DMT1 cells. (E) Technical and biological verifications by qRT-PCR analyses in HEK-293 and HEK-293 DMT1 cells upon treatment with Pb^{2+} or Pb^{2+} plus *C. vulgaris* aqueous extract. IPA predicted cellular functions in Pb^{2+}-exposed (F) HEK-293 cells and (G) HEK-293 DMT1 cells. IPA predicted diseases in Pb^{2+}-exposed (H) HEK-293 cells and (I) HEK-293 DMT1 cells.

Metabolic pathways in HEK-293 DMT1 cells as predicted by IPA

To further investigate these observations in HEK-293 DMT1 cells, we examined the canonical pathway classifications in IPA, which group pathways into signaling pathways, reactome pathways, and metabolic pathways. The analysis of the ratio of the number of overlapping genes to the total number of genes in the pathway revealed that both Pb^{2+} exposure and *C. vulgaris* treatment produced the highest overlap ratios (0.5) in the metabolic pathways compared with signaling and reactome pathways in HEK-293 DMT1 cells (Fig. 6A and B). Notably, the metabolic pathways in both groups were primarily associated with degradation/utilization/assimilation, detoxification, and biosynthesis.

In Pb^{2+}-exposed HEK-293 DMT1 cells, predicted metabolic alterations indicate that degradation/utilization/assimilation pathways are primarily associated with "Aspartate degradation II", "Glutamate degradation III", and "Heme degradation". Predicted detoxification responses are strongly linked to the "Glutamate-dependent acid resistance pathway", highlighting a potential cellular stress-adaptation mechanism. In addition, predicted biosynthesis is enriched in pathways related to "NAD salvage pathway III", "NAD biosynthesis III", "Palmitate biosynthesis I", "Lipoate biosynthesis and incorporation II", and "Choline biosynthesis III" (Supplementary Table S2), suggesting increased metabolic demand and cofactor remodeling upon Pb^{2+} stress. Furthermore, Pb^{2+}-exposed cells also showed significantly reduced expression of several degradation/utilization/assimilation markers, including *CTSB, TSG101*, and *VPS26A* (Fig. 6G). Meanwhile, the IPA-based network analysis revealed that the predicted inhibition of TCA cycle II was accompanied by a significant downregulation of the malate dehydrogenase gene (*MDH*) (Fig. 6E), suggesting that Pb^{2+} exposure alters basic energy and metabolic processes in HEK-293 DMT1 cells.

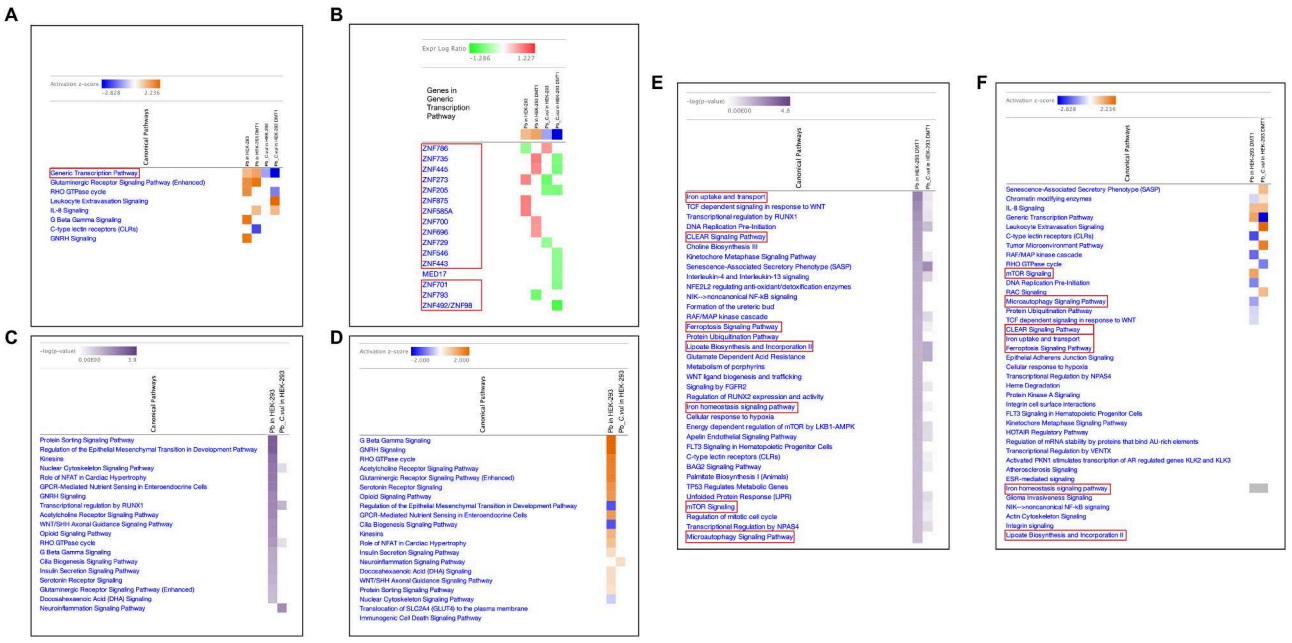


Fig. 5. Comparison of canonical pathways among the four experimental groups: Pb^{2+}-exposed HEK-293 cells, Pb^{2+}-exposed HEK-293 DMT1 cells, *C. vulgaris* -treated plus Pb^{2+}-exposed HEK-293 cells, and *C. vulgaris*-treated plus Pb^{2+}-exposed HEK-293 DMT1 cells in the QIAGEN Knowledge Base. (A) Prediction of activation or inhibition in the "Generic transcription pathway" by Z-score among the four experimental groups. (B) Heatmap of genes in the "Generic transcription pathway" by experimental log ratio among the four experimental groups. Heatmap of –log *p*-value and Z-score in canonical pathways between Pb^{2+}-exposed and *C. vulgaris* -treated plus Pb^{2+}-exposed (C-D) HEK-293 cells and (E-F) HEK-293 DMT1 cells.

Table 2
Canonical pathway comparison between the Pb^{2+}-exposed and *C. vulgaris*-treated Pb^{2+}-exposed HEK-293 DMT1 cells.

Canonical pathways	–log(*p*-value) upon Pb^{2+} exposure	–log(*p*-value) upon Pb^{2+} plus *C. vulgaris* treatment
Autophagy		
CLEAR signaling pathway	2.428*	-
mTOR signaling	1.630*	0.553
Microautophagy signaling pathway	1.593*	-
Ferroptosis		
Iron uptake and transport	3.102*	0.628
Iron homeostasis	1.827*	0.340
Ferroptosis signaling pathway	1.940*	0.365
Protein lipoylation		
Lipoate biosynthesis and incorporation II	1.854*	2.044*

Enrichment significance *p*-value is calculated using Fisher's exact test independent of regulation direction in IPA. A –log *p*-value > 1.3 is defined as statistically significant (*). -, pathway absence. IPA, ingenuity pathway analysis.

In contrast, in *C. vulgaris* water extract-treated Pb^{2+}-exposed HEK-293 DMT1 cells, predicted degradation/utilization/assimilation activity is predominantly linked to "Glutamate degradation III" (Supplementary Table S2). The predicted detoxification response remains centered on glutamate-dependent acid resistance, similar to Pb^{2+} exposure alone (Supplementary Table S2). However, the predicted biosynthesis profile shifts notably toward "Purine nucleotide *de novo* biosynthesis" and "Lipoate biosynthesis and incorporation II" (Supplementary Table S2), instead of the broader NAD- and lipid-focused biosynthesis in cells with Pb^{2+} alone. Supporting this shift, IPA analysis predicted an upregulation of HIF-1α in *C. vulgaris* water extract-treated Pb^{2+}-exposed HEK-293 DMT1 cells, a factor commonly activated during cellular stress and involved in metabolic adjustment (Fig. 6H). These results suggest that *C. vulgaris* water extract may help redirect the metabolic changes caused by Pb^{2+} exposure.

Metal transport pathways in HEK-293 DMT1 cells as predicted by IPA

In addition, evidence for disrupted molecular transport, a process closely associated with cellular rescue and stress response mechanisms (Martinez-Vicente et al., 2010; Ravikumar et al., 2010), was identified in HEK-293 DMT1 cells (–log *p*-value > 1.3, Fig. 4G). Among that, we emphasized the metal transport pathways. Pb^{2+} exposure led to targeted changes in eight genes associated with metal transport, upregulated genes, including *CNCNB4, KCNF1, SLC7A11, ATP6V0A2, HMOX1*, and *TMEM175*, whereas *TFR2* and *ATP7B* were downregulated (Fig. 6C). These genes encompass pathways involved in the transport of metal, the transport of heavy metal, homeostasis of transition metal ion, homeostasis of iron ion and export of heavy metal (Fig. 6C). Following *C. vulgaris* treatment, the number of differentially expressed metal transport genes decreased, with the increasing expression of *PTCH1, SLC16A1*, and *HMOX1* and decreasing expression of *ATP1B3* and *ATP7B* (Fig. 6D), which reflected a partial restoration of metal transport pathways. Furthermore, Pb^{2+} exposure also deregulated the expression of pH regulation-related genes, including *SLC16A1* downregulation and *ATP6V0A2* upregulation in the network of HEK-293 DMT1 cells (Fig. 6F), suggesting Pb^{2+}-induced disturbances in pH balance that may exacerbate metal-transport dysfunction, because metal transport is strongly pH-dependent (Kelly et al., 2003; Tariq et al., 2017).

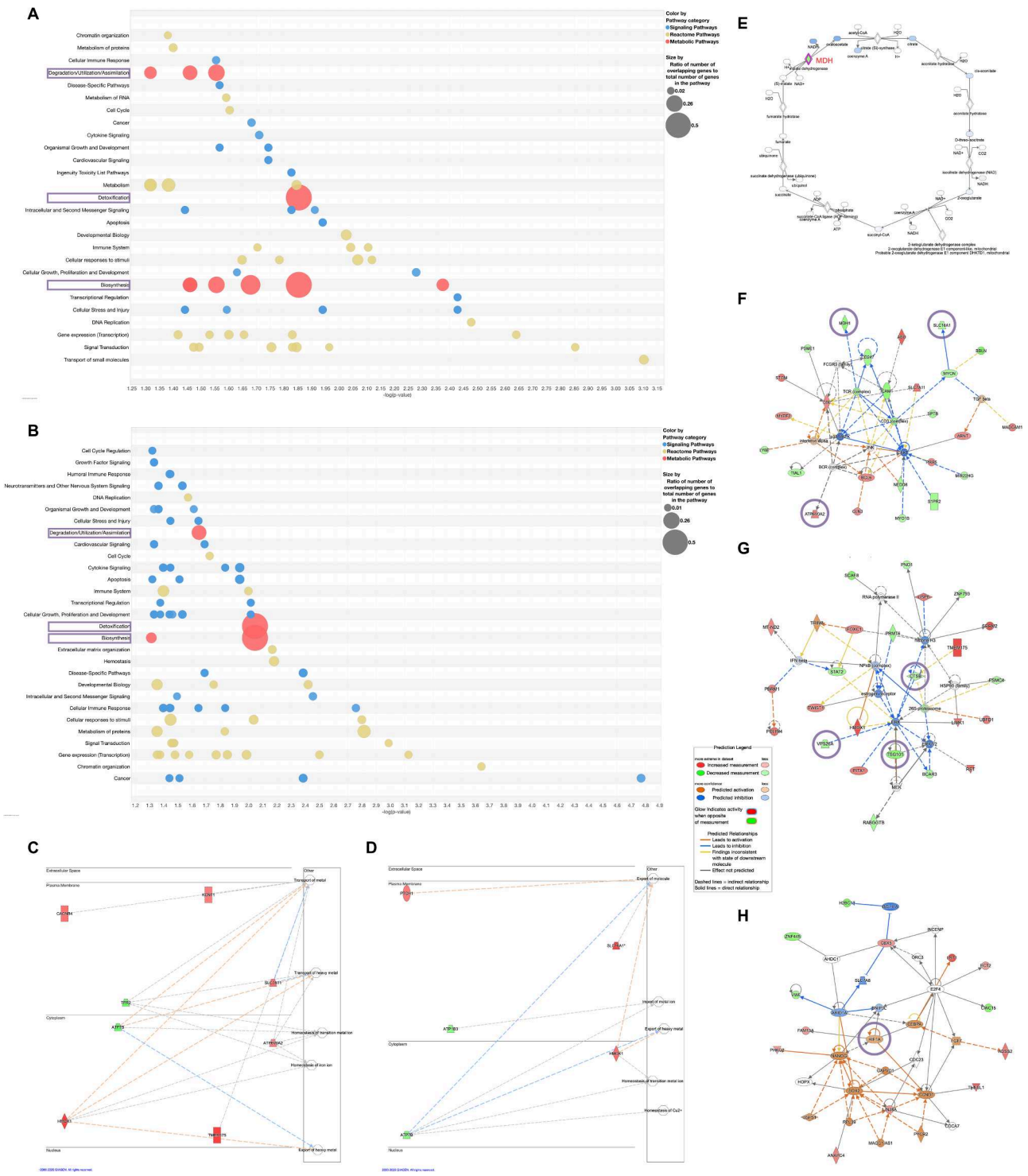


Fig. 6. IPA-based dot plot histograms depicting sub-pathways in metabolic, signaling, and reactome pathways in HEK-293 DMT1 cells between the (A) Pb^{2+}-exposed group and (B) *C. vulgaris*-treated plus Pb^{2+}-exposed group. Predicted metal transport gene network in (C) Pb^{2+}-exposed and (D) *C. vulgaris*-treated plus Pb^{2+}-exposed HEK-293 DMT1 cells. (E) Predicted inhibition of TCA cycle II in Pb^{2+}-exposed HEK-293 DMT1 cells. (F) Predicted functional network of Pb^{2+}-exposed HEK-293 DMT1 cells. The purple circles highlight the genes related to pH regulation. (G) Predicted functional network of Pb^{2+}-exposed HEK-293 DMT1 cells. The purple circles highlight the genes related to "Degradation/utilization/assimilation". (H) Predicted functional network of *C. vulgaris*-treated plus Pb^{2+}-exposed HEK-293 DMT1 cells. The purple circle highlights the gene related to "Cellular stress".

Chlorella reverses lead-triggered ferroptotic stress and impairments in autophagy pathways

To assess ferroptosis induced by lead, we evaluated cell viability in HEK-293 DMT1 cells treated with 0.3 μM Pb^{2+} alone and in combination with 0.5 μM of the iron chelator deferoxamine (DFO). As shown in Fig. 7A, deferoxamine markedly increased the IC_{50} of Pb^{2+} from 3.16 μM to 9.18 μM, representing a 2.9-fold change (Table 1), highlighting the critical role of iron in Pb^{2+}-induced cytotoxicity. Similarly, co-treatment with *C. vulgaris* water extract elevated the IC_{50} to 5.89 μM (Table 1),

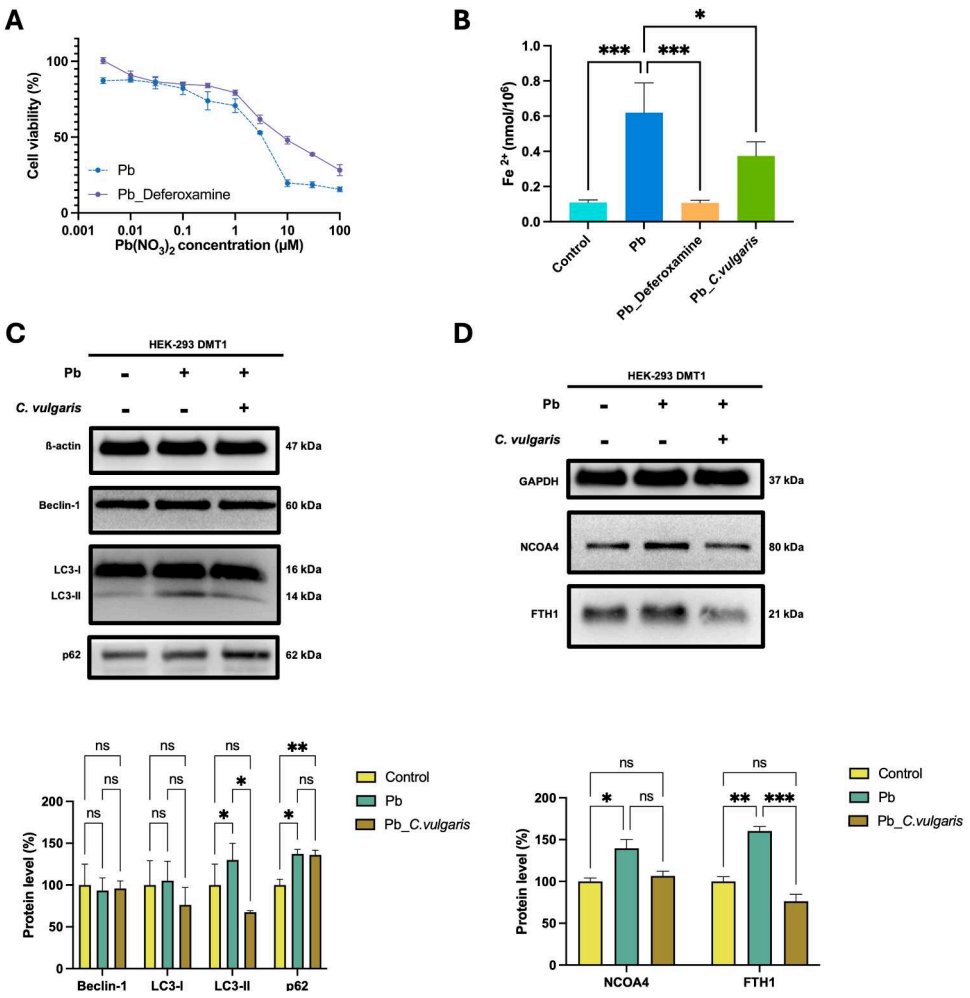


Fig. 7. *C. vulgaris* aqueous extract mitigates Pb^{2+}-induced ferroptotic stress and autophagy blockage. (A) Assessment of ferroptosis inhibition by deferoxamine during Pb^{2+} exposure in HEK-293 DMT1 cells. (B) Cellular ferrous iron (Fe^{2+}) levels in HEK-293 DMT1 cells incubated with Pb^{2+} alone and co-treatment with deferoxamine or *C. vulgaris* aqueous extract. The expression of (C) autophagy-related proteins and (D) ferritinophagy-related proteins in HEK-293 DMT1 cells incubated with Pb^{2+} in the presence or absence of *C. vulgaris* extract. All data (A-D) are represented as means ± SD (n=3). Statistical analyses were performed using one-way (B) or two-way (C-D) ANOVA followed by Tukey's post hoc. Not significant (ns), $*p < 0.05$, $**p < 0.01$, and $***p < 0.001$.

indicating a protective effect against Pb^{2+} toxicity. Given that ferrous iron (Fe^{2+}) is a key mediator of ferroptosis through catalysis of the Fenton reaction (Fang et al., 2021; Tang et al., 2021), we measured intracellular Fe^{2+} levels. Pb^{2+} exposure significantly increased Fe^{2+} compared to control ($p < 0.001$). Deferoxamine treatment effectively reduced Fe^{2+} levels relative to Pb^{2+} alone ($p < 0.001$), confirming iron chelation as a protective mechanism. Notably, *C. vulgaris* extract also significantly decreased Fe^{2+} levels compared with Pb^{2+} treatment ($p < 0.05$), further supporting its role in mitigating Pb^{2+}-induced ferroptotic stress (Fig. 7B).

We further investigated autophagy markers, as IPA pathway analysis identified them as highly relevant mechanism in Pb^{2+}-exposed HEK-293 DMT1 cells. The expression of Beclin-1, an upstream regulator of autophagosome formation, remained unchanged across all groups (Fig. 7C). In contrast, the autophagic flux markers LC3-II and p62 were significantly upregulated by Pb^{2+} exposure, indicating a blockade in the completion of autophagy (Fig. 7C). Co-treatment with *C. vulgaris* water extract significantly reduced LC3-II levels relative to Pb^{2+} alone, although p62 remained elevated, suggesting a partial restoration of autophagic flux (Fig. 7C).

Given the established role of ferroptosis and the critical interface between iron metabolism and autophagy, we hypothesized that Pb^{2+}-induced autophagy might specifically disrupt ferritinophagy. Therefore, we examined ferritinophagy by detecting the expression of its key mediator, NCOA4, and its cargo FTH1 (Fang et al., 2021). Pb^{2+} exposure significantly upregulated the expression of both NCOA4 and FTH1 in HEK-293 DMT1 cells ($p < 0.05$ and $p < 0.01$). This paired upregulation indicates a blocked ferritinophagic flux, by which the NCOA4-FTH1 complex accumulates (Fig. 7D). Crucially, co-treatment with C. *vulgaris* extract restored NCOA4 to near-basal levels and significantly reduced FTH1 accumulation ($p < 0.001$, Fig. 7D). These results indicate that *C. vulgaris* extract may mitigate Pb^{2+}-induced ferroptotic stress, likely through modulation of the NCOA4–FTH1-mediated ferritinophagy and restoring LC3-II/p62 associated autophagic flux.

Lead sensitizes HEK-293 DMT1 cells to Chlorella-induced suppression of protein lipoylation

We further found a clue of protein lipoylation in HEK-293 DMT1 cells using IPA. Pb^{2+} exposure induced the downregulation of copper-related genes. We observed a downregulation of *ATP7B* (ATPase Copper Transporting Beta) and *ATOX1* (Antioxidant 1 Copper Chaperone) (Fig. 8A). Meanwhile, the transcriptomic data indicated that Pb^{2+} exposure upregulated the expression of lipoic acid synthase (*LIAS*), whereas *LIAS* was significantly downregulated following *C. vulgaris* aqueous extract treatment (Fig. 8A and B). Alongside, co-treatment with *C. vulgaris* aqueous extract inhibited protein lipoylation, as predicted by IPA (Fig. 8C). Western blot analysis revealed a discrepancy between the

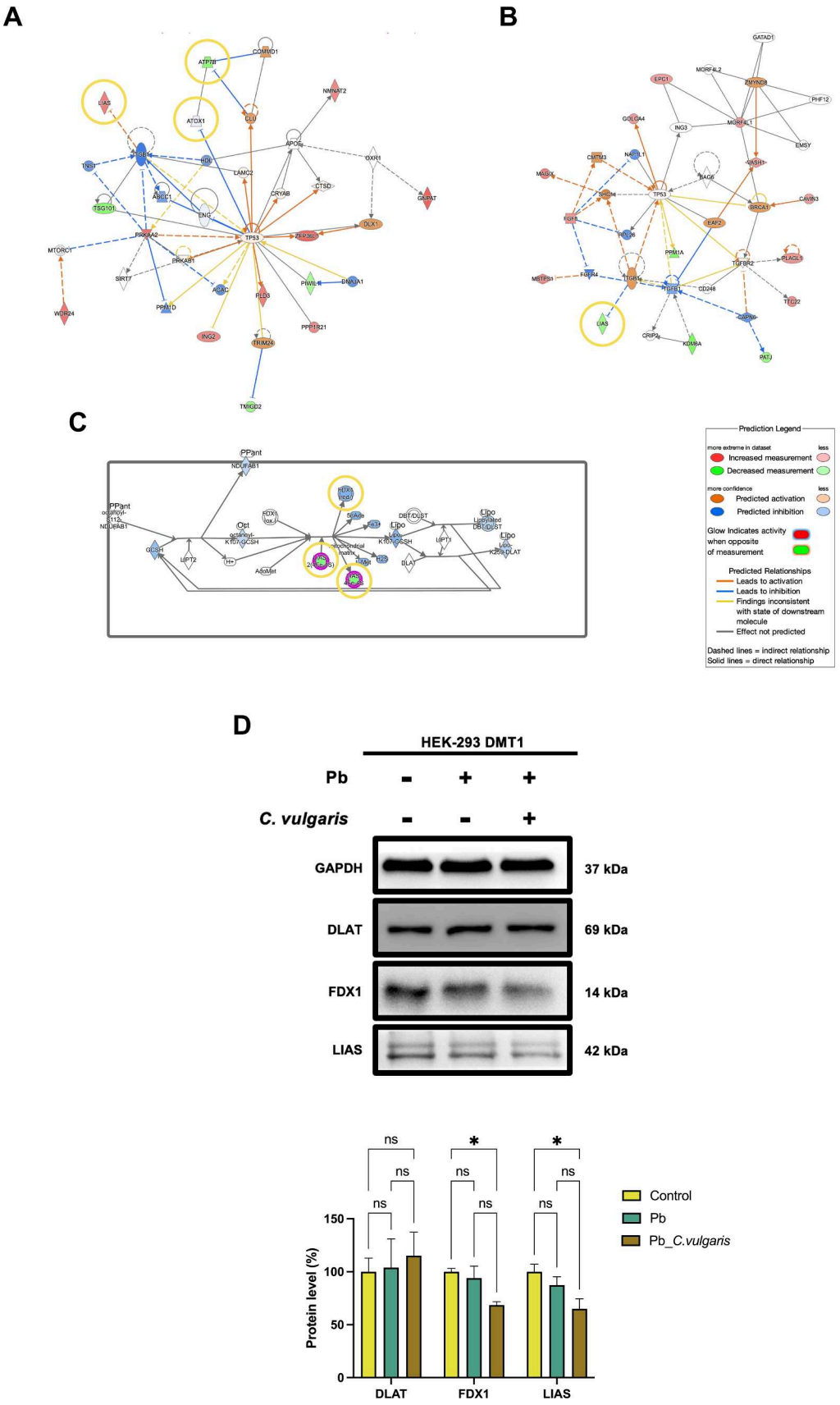


Fig. 8. Protein lipoylation is inhibited by *C. vulgaris* water extract only upon co-exposure with Pb^{2+}. Prediction of protein lipoylation-related network by IPA analysis of (A) Pb^{2+}-exposure and (B-C) co-treatment of *C. vulgaris* aqueous extract in HEK-293 DMT1 cells. The yellow circles highlight the genes related to protein lipoylation. (D) The expression of lipoylation-related proteins in HEK-293 DMT1 cells incubated with Pb^{2+} in the presence or absence of *C. vulgaris* aqueous extract. Data are represented as means ± SD (n=3). The statistical analyses were performed using two-way ANOVA followed by Tukey's post hoc. Not significant (ns), $*p < 0.05$.

transcriptome and protein levels of *LIAS* in the Pb^{2+}-exposed group. Specifically, Pb^{2+} alone failed to significantly increase LIAS protein expression compared with the control (Fig. 8D), suggesting a decline in functional LIAS protein. By contrast, FDX1 and LIAS protein expressions in the *C. vulgaris* water extract co-treated group mirrored the transcriptomic profile, showing significant downregulation ($p < 0.05$, Fig. 8D) compared with the control. This observation suggests that the inhibitory effect of the *C. vulgaris* extract on protein lipoylation may be specifically manifest in the presence of Pb^{2+} within DMT1-overexpressing HEK-293 cells.

An apoptosis-independent mechanism underlies C. vulgaris-mediated lead detoxification

Initial transcriptomic profiling via IPA indicated a potential mode of action of apoptosis in Pb^{2+}-exposed HEK-293 cells (Supplementary Fig. S2). Therefore, we examined key apoptotic proteins in HEK-293 cells and HEK-293 DMT1 cells. Contrary to the transcriptomic predictions, which suggested increased expression of caspase-3 and Bcl-xL, decreased PARP, no statistically significant changes in the protein levels of these markers were induced by Pb^{2+} in either cell line (Supplementary Fig. S2). As Pb^{2+} exposure did not establish an apoptotic state in our model, the subsequent evolution of *C. vulgaris* water extract had no significant effect on this pathway under these experimental conditions (Supplementary Fig. S2).

C. vulgaris counteracts lead-mediated inhibition of STAT3 phosphorylation and its microtubule regulatory function

Lastly, we sought to identify the key regulators underlying changes in cell proliferation. IPA analysis of *C. vulgaris* water extract–treated HEK-293 DMT1 cells revealed the upregulation of several cell growth– and immunity-related factors (*RELA, NFKB, CD4, TIPARP*, and *ICAM1*), along with predicted activation of additional signaling molecules (*ERK, AKT, JNK*, p38 *MAPK*, and *CD3*) (Fig. 9C). Importantly, *ICAM1* emerged as one of the most strongly upregulated genes, whereas Pb^{2+} exposure significantly suppressed its expression in HEK-293 DMT1 cells (Fig. 9A). Because STAT3 is a key transcriptional regulator of ICAM1 (Kesanakurti et al., 2013), we subsequently examined STAT3 expression and activation by western blotting. IPA also predicted that ICAM1 in Pb^{2+}-exposed cells was linked to disrupted microtubule polarization and impaired cell–cell contact (Fig. 9B), prompting us to assess microtubule organization by fluorescence microscopy.

Fig. 9D reveals that *C. vulgaris* water extract specifically counteracted the Pb^{2+}-induced suppression of STAT3 activity, as indicated by the restored phosphorylation at Tyr705, while total STAT3 expression remains unchanged. Intriguingly, this rescue of STAT3 signaling was accompanied by a significant decrease in the activation state of PI3K, marked by reduced p85 phosphorylation at Tyr458 (Fig. 9D). Thus, *C. vulgaris* extract rescued STAT3 signaling impaired by Pb^{2+} through a mechanism independent of, and perhaps counter to, the canonical PI3K pathway.

Fig. 9E illustrates the impact of Pb^{2+} exposure on the microtubule cytoskeleton. Control HEK-293 DMT1 cells displayed a characteristic, continuous network of polymerized microtubules, indicative of normal cytoskeletal integrity. This was abolished in vincristine-treated cells, which showed diffuse tubulin aggregation, confirming effective depolymerization. Pb^{2+} exposure induced a distinct pathological phenotype, characterized by microtubule destabilization and the formation of aberrant, stiff tubulin structures. Importantly, co-treatment with *C. vulgaris* water extract significantly mitigated these Pb^{2+}-induced defects, promoting a partial recovery toward a more extended and polymerized microtubule arrangement.

Discussion

Despite decades of research into lead detoxification since the 1940s, a critical bottleneck of chelating agents is still balancing the high efficacy with minimal adverse effects. *Chlorella* is a promising detoxification candidate that has been commercially used as a supplement due to its notable chelating capacity for heavy metals, as well as ancillary benefits, including antioxidant activity and cellular repair properties. However, an integrated picture of all biological mechanisms, how *Chlorella* orchestrates the lead detoxification, is still not fully defined. To address this gap, we targeted a critical endogenous protein, the DMT1 transporter, and combined genomic and functional cellular assays, delineating a mechanistic framework behind *Chlorella*-mediated lead detoxification.

We began by conducting a comparative metabolomic profiling of two dietary supplements, *C. vulgaris and C. pyrenoidosa,* to select the superior *Chlorella* species for our investigation. This revealed a prominent biochemical divergence between the species: flavonoids (luteolin, apigenin) and chlorophyll-derived porphyrins were detected exclusively in *C. vulgaris* extracts. This finding indicated that *C. vulgaris* possessed an enhanced biosynthesis capacity for valuable plant-derived antioxidant compounds and maintained a more active photosynthetic pigment cycle, underscoring its biochemical advantage over *C. pyrenoidosa* for our purpose. Moreover, FBMN networks further established that the metabolomic landscape of both species was lipid-dominated, with glycolipids, phospholipids, and free fatty acids constituting the major classes. Comprehensive UPLC-HRMS/MS-based metabolomic profile analyses confirmed that both species exhibited rich glycerophospholipid and glycerolipid profiles with high levels of unsaturated fatty acids, which is consistent with their established nutraceutical value. Given the unique secondary metabolite signature, particularly the key antioxidant flavonoids and porphyrins, we therefore selected *C. vulgaris* extracts for the subsequent experimental work.

Our next objective was to construct a tractable mechanistic model for assessing the protective molecular and cellular effects of *C. vulgaris* extracts. The results for antioxidant capacity revealed that the water extract of *C. vulgaris* was the most potent, which aligns with clinical evidence (Schilling et al., 2025). Importantly, this water extract also exhibited no cytotoxicity, affirming its biocompatibility. Subsequently, Pb^{2+} exhibited strong sensitivity towards DMT1-overexpressing cells compared to their wild-type cells, with a four-fold change in the IC_{50} value, confirming the Pb^{2+} uptake property of the DMT1 transporter. A preliminary screening of different concentrations showed that 30 μg/mL *C. vulgaris* water extract presented the best restoration of viability of DMT1-transfected cells upon treatment with a toxic concentration of 0.3 μM Pb^{2+} (data not shown). This combination treatment was subsequently used as an experimental model for studying molecular detoxification mechanisms.

Following model validation, we initially investigated the direct action of *C. vulgaris* water extract on Pb^{2+} by detecting intracellular and extracellular Pb^{2+} concentrations over a time course. The results pointed to enhanced Pb^{2+} export as the predominant mode of action of *C. vulgaris* water extract, with a secondary contribution from the attenuation of cellular uptake. *C. vulgaris* water extract showed significant efflux of Pb^{2+} after 8 h, nearly that of the well-known lead chelator EDTA-$CaNa_2$. Although its ultimate chelation efficacy is weaker than that of EDTA-$CaNa_2$, it lacks the considerable drawbacks of EDTA-$CaNa_2$, *i.e.*, renal toxicity, and promotes essential mineral depletion (Fishbane and Maesaka, 1997; Gutiérrez, 2021). This highlights a critical therapeutic distinction, which may be paramount for long-term or preventative nutraceutical applications.

Next, we proceeded with the transcriptomic analysis to map the cellular pathways dysregulated by Pb^{2+}. Pb^{2+}-exposed DMT1-transfected cells revealed a striking shift in transcriptomic toxicity profiles, while wild-type HEK-293 cells displayed a profile specifically on cardiotoxicity, hepatic toxicity, and renal toxicity. DMT1-

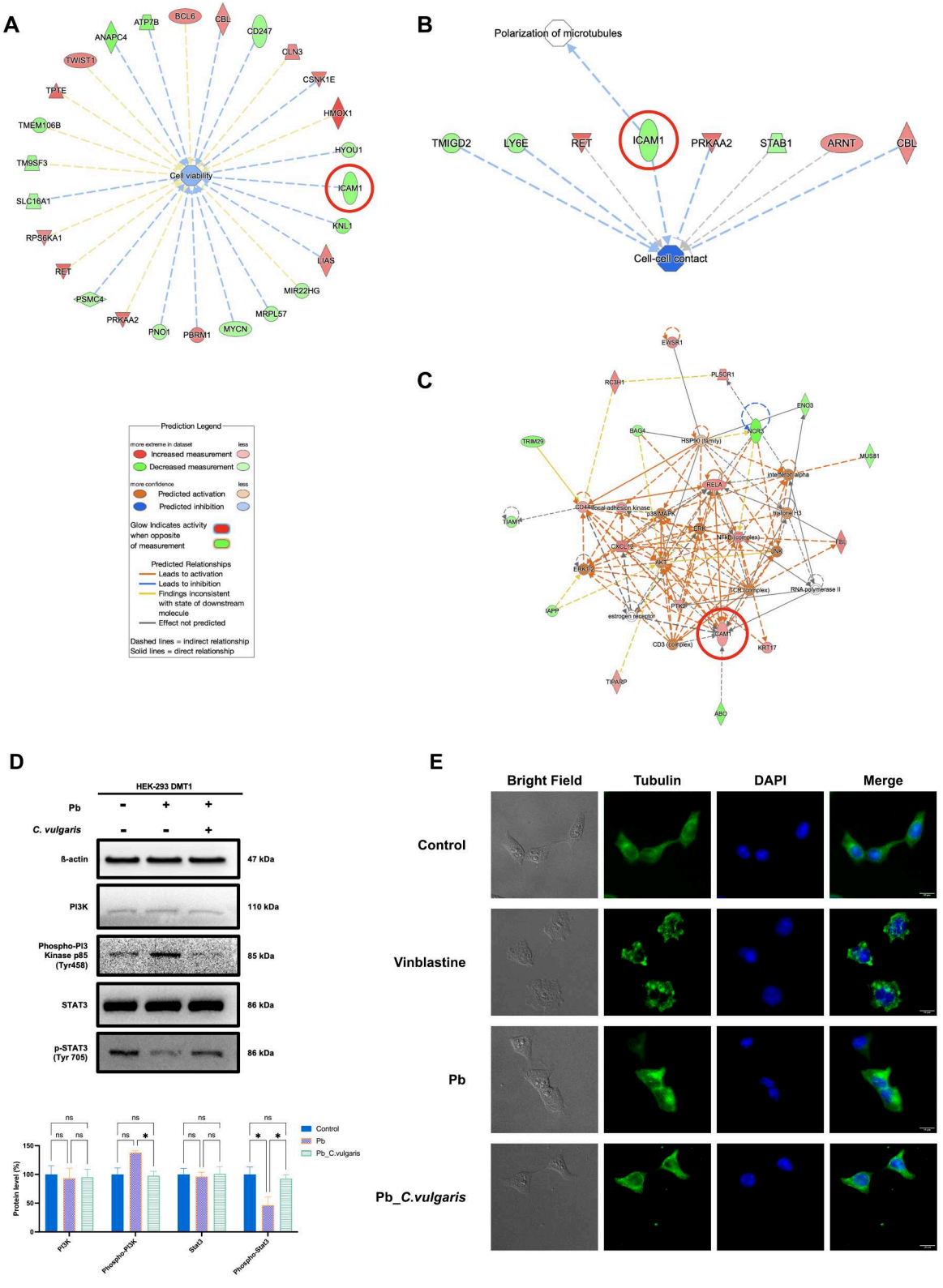


Fig. 9. *C. vulgaris* mitigates Pb^{2+}-induced loss of STAT3 phosphorylation and microtubule stability mechanisms. (A-B) Prediction of functional network by IPA of Pb^{2+}-exposed HEK-293 DMT1 cells. (C) Prediction of functional network by IPA of co-treatment of *C. vulgaris* plus Pb^{2+} exposure in HEK-293 DMT1 cells. The red circles highlight the genes related to STAT3 signaling. (D) Western blotting analysis of STAT3-related signaling in HEK-293 DMT1 cells following Pb^{2+} exposure or co-treatment with *C. vulgaris* aqueous extract. (E) Immunofluorescence imaging of the microtubule network (β-tubulin, green) following indicated treatments. Nuclei were counterstained with DAPI (blue). Images were acquired at 40× magnification (scale bar = 10 μm). Data are represented as means ± SD (n=3). The statistical analyses were performed using two-way ANOVA followed by Tukey's post hoc. Not significant (ns), *$p < 0.05$.

overexpressing cells exhibited a signature of hepatic and renal toxicity, which suggested that DMT1-mediated Pb^{2+} transport preferentially induced hepatorenal toxicity. The toxicity in wild-type cells likely reflected lead-induced accumulation of lipid hydroperoxides (Chen et al., 2021), a mechanism shared with the iron-catalyzed Fenton reaction in cardiac toxicity (Hašková et al., 2011). In contrast, the refined hepatorenal toxicity in sensitized cells suggested a disruption of iron homeostasis. Mechanistically, this is corroborated by the Pb^{2+}-induced lipopolysaccharide biosynthesis pathway in hepatic metabolic disorders (Miao et al., 2023) and the fundamental role of iron in the regulation of hepatic lipogenesis (Gao et al., 2022), indicating that Pb^{2+}-induced liver toxicity is tightly associated with iron homeostasis (Gao et al., 2022; Liu et al., 2023). Furthermore, iron homeostasis is crucial for treating patients with anemia caused by end-stage renal disease (Fishbane and Maesaka, 1997; Gutiérrez, 2021). Given iron's essential role in erythropoiesis. Collectively, our transcriptome analysis implied that Pb^{2+} toxicity, if amplified by DMT1, converged on the disruption of iron homeostasis as a pivotal mechanism underlying its hepatorenal toxicity.

Remarkably, the canonical pathway analysis revealed that in wild-type and DMT1-transfected cells, *C. vulgaris* water extract counteracted Pb^{2+}-induced activation of the generic transcription pathway, with a more pronounced effect in DMT1-overexpressing cells. Intriguingly, this pathway is predominantly regulated by zinc finger proteins (ZFPs). Pb^{2+} ions are well-known for disturbing the DNA-binding properties of ZFPs by substituting the natural Zn^{2+} ions (Huang et al., 2004; Payne et al., 1999). While no prior study has linked *Chlorella* to the remediation of ZFP dysfunction, our data provided the first evidence that *C. vulgaris* water extract may act through a novel potential detoxification axis: the rescue of ZFP-mediated transcriptional homeostasis to attenuate Pb^{2+} toxicity.

Canonical pathway analysis in DMT1-overexpressing cells also indicated that *C. vulgaris* water extract ameliorates Pb^{2+} toxicity linked to two specific cell death pathways: autophagy and ferroptosis based on significance value comparisons. We focused first on the autophagic pathway. Pb^{2+} exposure is known to disrupt cellular recycling through autophagy, frequently by blocking autophagic flux at the lysosome stage, leading to accumulation of autophagosomes and subsequent cell damage (apoptosis) (Song et al., 2017), though sometimes autophagy is initially activated as a protective response. Consistent with this, our western blot analysis of Pb^{2+}-exposed DMT1-overexpressing cells showed a clear autophagic flux blockage, indicated by the concurrent upregulation of LC3-II and p62, while upstream marker Beclin-1 was unchanged. Notably, in our model, this concentration of Pb^{2+} has not triggered apoptosis yet (verified by western blot analysis of caspase-3, PARP, and Bcl-xL). Importantly, co-treatment with *C. vulgaris* water extract effectively reversed this blockage by normalizing LC3-II and p62. Together, these results demonstrated that *C. vulgaris* water extract may specifically alleviate Pb^{2+}-induced autophagic dysfunction, identifying the restoration of cellular recycling as a detoxification mechanism.

Research into Pb^{2+}-induced ferroptosis is in its infancy, but a proposed mechanism involves Pb^{2+}-mediated inhibition of system Xc− and glutathione depletion (Niu et al., 2025; Shi et al., 2023). In our study, the resazurin reduction assay with co-treated deferoxamine suggested Pb^{2+} induced ferroptosis, which was further supported by ferrous iron level detection, both consistent with ferroptosis. Notably, *C. vulgaris* water extract concurrently suppressed this ferroptotic response, significantly reducing ferrous iron levels and restoring cell viability. Delving into the iron metabolism underpinning this effect, we found that Pb^{2+} potentially disturbed ferrotinophagy via western blotting. Specifically, Pb^{2+} upregulated *NCOA4*, marking the initiation of ferritin turnover, and *FTH1*, a core component of the iron-storage ferritin complex. We interpret this paradoxical upregulation as a failed homeostatic circuit: NCOA4 elevation-initiated ferritin degradation, while the elevated FTH1 may be an attempt to buffer cytotoxic labile iron. This imbalance, potentially exacerbated by the broader autophagic flux blockage we observed, signified a profound disturbance in iron homeostasis. The pivotal finding is that *C. vulgaris* water extract may normalize this dysregulation, reverting *NCOA4* and *FTH1* toward control levels. These findings suggested that ameliorating aberrant ferritinophagy and iron handling is a key mechanism through which *C. vulgaris* water extract counteracted Pb^{2+}-induced ferroptotic stress.

Unexpectedly, *LIAS* expression exhibited a discordance between transcript abundance and protein level following DMT1-mediated Pb^{2+} stress, pointing to a reduction in functional LIAS protein. This discordance likely arises from two opposing mechanisms: lead stress triggers compensatory *LIAS* transcription, yet disrupted iron homeostasis may lead to loss of LIAS iron-sulfur clusters (Hendricks et al., 2021), destabilizing the protein for degradation. Ultimately, the transcriptional upregulation is offset by protein degradation, yielding no significant change in protein levels. Next, we observed a specific suppression of protein lipoylation by *C. vulgaris* water extract in Pb^{2+}-sensitized HEK-293 DMT1 cells, as confirmed by the significant downregulation of both FDX1 and LIAS. To our knowledge, no prior study has investigated whether *Chlorella* modulates protein lipoylation as a potential detoxification pathway to Pb^{2+}. This essential post-translational modification could funnel carbon into the TCA cycle to fuel energy production (Lin et al., 2024). Its inhibition suggested a strategic metabolic rewiring by the *C. vulgaris* water extract. This may initiate a well-characterized cascade: impairment of the TCA cycle reduces α-ketoglutarate (α-KG) and promotes L-2-hydroxyglutarate (L-2-HG) accumulation, resulting in prolyl-hydroxylase (PHD) inhibition and hypoxia-inducible factor 1α (HIF-1α) stabilization (Martínez-Reyes and Chandel, 2020), further driving metabolic adaptation pathways to establish a new, protective homeostasis upon lead-induced stress. Metabolic pathway prediction further supported a shift toward an adaptive biosynthetic profile by *C. vulgaris* water extract, notably enriched in purine nucleotide *de novo* biosynthesis, instead of the broader NAD- and lipid-focused biosynthesis in Pb^{2+}-exposed cells, which supports the metabolic adaptation strategy at the transcriptomic level.

Regarding pathways governing cell survival, its restoration by *C. vulgaris* water extract was critically associated with the modulation of phosphorylated STAT3 signaling and a concomitant recovery of microtubules toward a more extended and polymerized arrangement. These observations align with previous studies, which show that STAT3 suppresses ferroptosis in gastric cancer (Ouyang et al., 2022) and promotes the stabilization of microtubules (Ng et al., 2006). Therefore, the *C. vulgaris* water extract likely mitigates Pb^{2+} toxicity via a coordinated action on the p-STAT3 pathway, concurrently inhibiting ferroptosis and stabilizing the microtubule network. Additionally, a synergistic interaction may exist between the two bioactive flavonoids present in the *C. vulgaris* aqueous extract. Luteolin is a more effective lead chelator (Wang et al., 2019) than apigenin, yet it is metabolized faster in animal models (Chen et al., 2012). Notably, in rat hepatocytes, the drug-drug interactions between luteolin and apigenin reduced the elimination of both compared to their pure forms (Lu et al., 2011), suggesting synergy. For further *in vivo* test, intestinal enterocytes are a recommended focus, given that DMT1-iron uptake, STAT3-epithelial repair, and certain ZFPs-transcription factors governing renewal, are all integral to their function (Arredondo et al., 2003; Wittkopf et al., 2015; Xie et al., 2022).

Conclusions

This work established that *C. vulgaris* water extract potentially mediated a coordinated network against Pb^{2+} toxicity. We uncovered a putative multi-layered detoxification defense: it was prone to promote cellular metal export rather than inhibit import, rectified specific Pb^{2+}-induced damages, re-established autophagic flux, and modulated ferroptotic stress through iron homeostasis regulation. Concurrently, it may drive an adaptive metabolic program via protein lipoylation, activate pro-survival STAT3 signaling, and restore microtubule stability, thereby fortifying cellular integrity. Ultimately, we underscore the utility of *C. vulgaris* as a natural countermeasure to Pb^{2+} toxicity and its

potential as a nutraceutical adjuvant in lead detoxification.

Editor conflict of interest statement

Given my role as Editor-in-Chief, we confirm that I am not involved in the peer-review of the article mentioned below, and that I do not interfere with the process of peer-review:

Deciphering the complex mechanisms of action of lead detoxification by the green microalgae *Chlorella vulgaris*.

CRediT authorship contribution statement

Chunmei Jin: Writing – original draft, Methodology, Investigation, Formal analysis, Data curation. **Seren Gündoğdu:** Writing – original draft, Investigation, Formal analysis, Data curation. **Nesrine M. Hegazi:** Writing – original draft, Investigation, Formal analysis. **Xiaohua Lu:** Writing – review & editing, Validation. **Mohamed Elbadawi:** Writing – review & editing, Validation. **Christopher Kampf:** Investigation. **Sabine M Klauck:** Writing – review & editing, Investigation. **Sarra Rahali:** Investigation. **Nico Achenbach:** Investigation. **Mohamed-Elamir F. Hegazy:** Writing – review & editing, Writing – original draft, Formal analysis, Data curation, Conceptualization. **Thomas Efferth:** Writing – review & editing, Writing – original draft, Supervision, Resources, Project administration, Methodology, Funding acquisition, Conceptualization.

Declaration of competing interest

The authors declare that they have no known competing financial interests or personal relationships that could have appeared to influence the work reported in this paper.

Acknowledgments

We thank the Microarray Unit of the Genomics and Proteomics Core Facility, German Cancer Research Center (DKFZ), Heidelberg, for providing excellent expression profiling services. Mohamed-Elamir F. Hegazy acknowledges the financial support of the Alexander von Humboldt Foundation, Germany, through the Research Group Linkage Programme. We sincerely thank Prof. Matthias A. Hediger from the University of Bern for generously providing the HEK-293 and HEK-293 DMT1 cells. We acknowledge the valuable support of the IMB (Institute of Molecular Biology, Mainz, Germany) Microscopy Core Facility for the fluorescence imaging. We are grateful for a Ph.D. stipend from the Chinese Scholarship Council (CSC) to C.J, an Overseas Doctoral Research Fellowship Program from the Scientific and Technological Research Council of Türkiye (TUBITAK) to S.G. This project was funded by a private donation of Marc Strobel, Frankfurt, Germany. The graphical abstract was created in BioRender. Jin, C. (2026) https://BioRender.com/evzlatr.

Supplementary materials

Supplementary material associated with this article can be found in the online version, at doi:10.1016/j.phymed.2026.158349.

References

Abdalla, F.H., Bellé, L.P., De Bona, K.S., Bitencourt, P.E.R., Pigatto, A.S., Moretto, M.B., 2010. *Allium sativum* L. extract prevents methyl mercury-induced cytotoxicity in peripheral blood leukocytes (LS). Food Chem. Toxicol. 48, 417–421. https://doi.org/10.1016/j.fct.2009.10.033.

Aga, M., Iwaki, K., Ueda, Y., Ushio, S., Masaki, N., Fukuda, S., Kimoto, T., Ikeda, M., Kurimoto, M., 2001. Preventive effect of *Coriandrum sativum* (Chinese parsley) on localized lead deposition in ICR mice. J. Ethnopharmacol. 77, 203–208. https://doi.org/10.1016/s0378-8741(01)00299-9.

Arredondo, M., Muñoz, P., Mura, C.V., Núñez, M.T., 2003. DMT1, a physiologically relevant apical Cu^{1+} transporter of intestinal cells. Am. J. Physiol. Cell Physiol. 284, 1525–1530. https://doi.org/10.1152/ajpcell.00480.2002.

Bajguz, A., 2011. Suppression of *Chlorella vulgaris* growth by cadmium, lead, and copper stress and its restoration by endogenous brassinolide. Arch. Environ. Contam. Toxicol. 60, 406–416. https://doi.org/10.1007/s00244-010-9551-0.

Bandaru, L.J.M., Ayyalasomayajula, N., Murumulla, L., Challa, S., 2022. Mechanisms associated with the dysregulation of mitochondrial function due to lead exposure and possible implications on the development of Alzheimer's disease. BioMetals 35, 1–25. https://doi.org/10.1007/s10534-021-00360-7.

Bannon, D.I., Portnoy, M.E., Olivi, L., Lees, P.S.J., Culotta, V.C., Bressler, J.P., 2002. Uptake of lead and iron by divalent metal transporter 1 in yeast and mammalian cells. Biochem. Biophys. Res. Commun. 295, 978–984. https://doi.org/10.1016/s0006-291x(02)00756-8.

Bressler, J.P., Olivi, L., Cheong, J.H., Kim, Y., Bannon, D., 2004. Divalent metal transporter 1 in lead and cadmium transport. Ann. N. Y. Acad. Sci. 1012, 142–152. https://doi.org/10.1196/annals.1306.011.

Buc, H.-A., Kaplan, J.-C., 1978. Red-cell pyrimidine 5'-nucleotidase and lead poisoning. Clin. Chim. Acta 87, 49–55. https://doi.org/10.1016/0009-8981(78)90056-6.

Chen, Z., Huo, X., Chen, G., Luo, X., Xu, X., 2021. Lead (Pb) exposure and heart failure risk. Environ. Sci. Pollut. Res. 28, 28833–28847. https://doi.org/10.1007/s11356-021-13725-9/Published.

Chen, Z., Tu, M., Sun, S., Kong, S., Wang, Y., Ye, J., Li, L., Zeng, S., Jiang, H., 2012. The exposure of luteolin is much lower than that of apigenin in oral administration of Flos Chrysanthemi extract to rats. Drug Metab. Pharmacokinet. 27, 162–168. https://doi.org/10.2133/dmpk.dmpk-11-rg-081.

Dührkop, K., Fleischauer, M., Ludwig, M., Aksenov, A.A., Melnik, A.V., Meusel, M., Dorrestein, P.C., Rousu, J., Böcker, S., 2019. SIRIUS 4: a rapid tool for turning tandem mass spectra into metabolite structure information. Nat. Methods 16, 299–302. https://doi.org/10.1038/s41592-019-0344-8.

Ettinger, A.S., Hu, H., Hernandez-Avila, M., 2007. Dietary calcium supplementation to lower blood lead levels in pregnancy and lactation. J. Nutr. Biochem. 18, 172–178. https://doi.org/10.1016/j.jnutbio.2006.12.007.

Fang, Y., Chen, X., Tan, Q., Zhou, H., Xu, J., Gu, Q., 2021. Inhibiting ferroptosis through disrupting the NCOA4-FTH1 interaction: a new mechanism of action. ACS Cent. Sci. 7, 980–989. https://doi.org/10.1021/acscentsci.0c01592.

Fenga, C., Gangemi, S., Di Salvatore, V., Falzone, L., Libra, M., 2017. Immunological effects of occupational exposure to lead (review). Mol. Med. Rep. 15, 3355–3360. https://doi.org/10.3892/mmr.2017.6381.

Fishbane, S., Maesaka, J.K., 1997. Iron management in end-stage renal disease. Am. J. Kidney Dis. 29, 319–333. https://doi.org/10.1016/s0272-6386(97)90192-x.

Fu, Z., Xi, S., 2020. The effects of heavy metals on human metabolism. Toxicol. Mech. Methods 30, 167–176. https://doi.org/10.1080/15376516.2019.1701594.

Gabrelian, M., Eugene Kimbrough, D., Kingston, H., Kocherlakota, N., Neuin, D., Tatro, M.E., Ultis, M.M., Weekley, M., Weiss, A.D., Wolf, R.E., 2004. 3030 preliminary treatment of samples. Standard Methods. American Public Health Association (APHA), American Water Works Association (AWWA), Water Environment Federation (WEF), pp. 1–8. https://doi.org/10.2105/SMWW.2882.041.

Gao, H., Jin, Z., Bandyopadhyay, G., Wang, G., Zhang, D., Rocha, K.C.E., Liu, X., Zhao, H., Kisseleva, T., Brenner, D.A., Karin, M., Ying, W., 2022. Aberrant iron distribution via hepatocyte-stellate cell axis drives liver lipogenesis and fibrosis. Cell Metab. 34, 1201–1213. https://doi.org/10.1016/j.cmet.2022.07.006.

Gutiérrez, O.M., 2021. Treatment of iron deficiency anemia in CKD and end-stage kidney disease. Kidney Int. Rep. 6, 2261–2269. https://doi.org/10.1016/j.ekir.2021.05.020.

Hašková, P., Kovaříková, P., Koubková, L., Vávrová, A., MacKová, E., Šimůnek, T., 2011. Iron chelation with salicylaldehyde isonicotinoyl hydrazone protects against catecholamine autoxidation and cardiotoxicity. Free Radic. Biol. Med. 50, 537–549. https://doi.org/10.1016/j.freeradbiomed.2010.12.004.

Hegazi, N., Khattab, A.R., Saad, H.H., Abib, B., Farag, M.A., 2024. A multiplex metabolomic approach for quality control of Spirulina supplement and its allied microalgae (*Amphora* and *Chlorella*) assisted by chemometrics and molecular networking. Sci. Rep. 14, 2809. https://doi.org/10.1038/s41598-024-53219-5.

Hegazi, N.M., Radwan, R.A., Bakry, S.M., Saad, H.H., 2020. Molecular networking aided metabolomic profiling of beet leaves using three extraction solvents and in relation to its anti-obesity effects. J. Adv. Res. 24, 545–555. https://doi.org/10.1016/j.jare.2020.06.001.

Hegazi, N.M., Saad, H.H., Marzouk, M.M., Abdel Rahman, M.F., El Bishbishy, M.H., Zayed, A., Ulber, R., Ezzat, S.M., 2021. Molecular networking leveraging the secondary metabolomes space of *Halophila stipulaceae* (Forsk.) Aschers. and *Thalassia hemprichii* (Ehrenb. ex Solms) Asch. in tandem with their chemosystematics and antidiabetic potentials. Mar. Drugs 19, 279. https://doi.org/10.3390/md19050279.

Hegazy, M.E.F., Dawood, M., Mahmoud, N., Elbadawi, M., Sugimoto, Y., Klauck, S.M., Mohamed, N., Efferth, T., 2021. 2α-hydroxyalantolactone from *Pulicaria undulata*: activity against multidrug-resistant tumor cells and modes of action. Phytomedicine 81, 153409. https://doi.org/10.1016/J.PHYMED.2020.153409.

Hemmaphan, S., Bordeerat, N.K., 2022. Reduced DNA glycosylases expression and oxidative DNA damage induced by lead. Toxicol. Int. 29, 321–328. https://doi.org/10.18311/ti/2022/v29i3/29322.

Hendricks, A.L., Wachnowsky, C., Fries, B., Fidai, I., Cowan, J.A., 2021. Characterization and reconstitution of human lipoyl synthase (LIAS) supports ISCA2 and ISCU as primary cluster donors and an ordered mechanism of cluster assembly. Int. J. Mol. Sci. 22, 1598. https://doi.org/10.3390/ijms22041598.

Hoet, P., Haufroid, V., Lison, D., 2020. Heavy metal chelation tests: the misleading and hazardous promise. Arch. Toxicol. 94, 2893–2896. https://doi.org/10.1007/s00204-020-02847-7.

Huang, M., Krepkiy, D., Hu, W., Petering, D.H., 2004. Zn-, Cd-, and Pb-transcription factor IIIA: properties, DNA binding, and comparison with TFIIIA-finger 3 metal complexes. J. Inorg. Biochem. 98, 775–785. https://doi.org/10.1016/j.jinorgbio.2004.01.014.

Kanti Das, T., Wati, M.R., Fatima-Shad, K., 2014. Oxidative stress gated by Fenton and Haber Weiss reactions and its association with Alzheimer's disease. Arch. Neurosci. 2, e20078. https://doi.org/10.5812/archneurosci.20078.

Kelly, C.A., Rudd, J.W.M., Holoka, M.H., 2003. Effect of ph on mercury uptake by an aquatic bacterium: implications for Hg cycling. Environ. Sci. Technol. 37, 2941–2946. https://doi.org/10.1021/es026366o.

Kesanakurti, D., Chetty, C., Rajasekhar Maddirela, D., Gujrati, M., Rao, J.S., 2013. Essential role of cooperative NF-κB and Stat3 recruitment to ICAM-1 intronic consensus elements in the regulation of radiation-induced invasion and migration in glioma. Oncogene 32, 5144–5155. https://doi.org/10.1038/onc.2012.546.

Kim, J.J., Kim, Y.S., Kumar, V., 2019. Heavy metal toxicity: an update of chelating therapeutic strategies. J. Trace Elem. Med. Biol. 54, 226–231. https://doi.org/10.1016/j.jtemb.2019.05.003.

Krämer, A., Green, J., Pollard, J., Tugendreich, S., 2014. Causal analysis approaches in ingenuity pathway analysis. Bioinformatics 30, 523–530. https://doi.org/10.1093/bioinformatics/btt703.

Lin, C.H., Chin, Y., Zhou, M., Sobol, R.W., Hung, M.C., Tan, M., 2024. Protein lipoylation: mitochondria, cuproptosis, and beyond. Trends Biochem. Sci. 49, 729–744. https://doi.org/10.1016/j.tibs.2024.04.002.

Liu, Y., Li, G., Lu, F., Guo, Z., Cai, S., Huo, T., 2023. Excess iron intake induced liver injury: the role of gut-liver axis and therapeutic potential. Biomed. Pharmacother. 168, 115728. https://doi.org/10.1016/j.biopha.2023.115728.

Livak, K.J., Schmittgen, T.D., 2001. Analysis of relative gene expression data using real-time quantitative PCR and the $2^{-\Delta\Delta CT}$ method. Methods 25, 402–408. https://doi.org/10.1006/METH.2001.1262.

Lu, X., Sun, D., Chen, Z., Ye, J., Wang, R., Li, L., Zeng, S., Jiang, H., 2011. Evaluation of hepatic clearance and drug-drug interactions of luteolin and apigenin by using primary cultured rat hepatocytes. Pharmazie 66, 600–605. https://doi.org/10.1691/ph.2011.1517.

Maciel, E., Leal, M.C., Lillebø, A.I., Domingues, P., Domingues, M.R., Calado, R., 2016. Bioprospecting of marine macrophytes using MS-based lipidomics as a new approach. Mar. Drugs 14, 49. https://doi.org/10.3390/md14030049.

Martínez-Reyes, I., Chandel, N.S., 2020. Mitochondrial TCA cycle metabolites control physiology and disease. Nat. Commun. 11, 102. https://doi.org/10.1038/s41467-019-13668-3.

Martinez-Vicente, M., Talloczy, Z., Wong, E., Tang, G., Koga, H., Kaushik, S., De Vries, R., Arias, E., Harris, S., Sulzer, D., Cuervo, A.M., 2010. Cargo recognition failure is responsible for inefficient autophagy in Huntington's disease. Nat. Neurosci. 13, 567–576. https://doi.org/10.1038/nn.2528.

Mbaveng, A.T., Bitchagno, G.T.M., Kuete, V., Tane, P., Efferth, T., 2019. Cytotoxicity of ungeremine towards multi-factorial drug resistant cancer cells and induction of apoptosis, ferroptosis, necroptosis and autophagy. Phytomedicine 60, 152832. https://doi.org/10.1016/j.phymed.2019.152832.

Mei, Z., Liu, G., Zhao, B., He, Z., Gu, S., 2023. Emerging roles of epigenetics in lead-induced neurotoxicity. Environ. Int. 181, 108253. https://doi.org/10.1016/j.envint.2023.108253.

Melo, T., Alves, E., Azevedo, V., Martins, A.S., Neves, B., Domingues, P., Calado, R., Abreu, M.H., Domingues, M.R., 2015. Lipidomics as a new approach for the bioprospecting of marine macroalgae - unraveling the polar lipid and fatty acid composition of *Chondrus crispus*. Algal Res. 8, 181–191. https://doi.org/10.1016/j.algal.2015.02.016.

Miao, Z., Miao, Z., Teng, X., Xu, S., 2023. Melatonin alleviates lead-induced fatty liver in the common carps (*Cyprinus carpio*) via gut-liver axis. Environ. Pollut. 317, 120730. https://doi.org/10.1016/j.envpol.2022.120730.

Mishima, E., Nakamura, T., Doll, S., Proneth, B., Fedorova, M., Pratt, D.A., Friedmann Angeli, J.P., Dixon, S.J., Wahida, A., Conrad, M., 2025. Recommendations for robust and reproducible research on ferroptosis. Nat. Rev. Mol. Cell Biol. 26, 615–630. https://doi.org/10.1038/s41580-025-00843-2.

Mishra, E., Worlinsky, J.L., Brückner, C., Ryzhov, V., 2014. MS/MS fragmentation behavior study of meso-phenylporphyrinoids containing nonpyrrolic heterocycles and meso-thienyl-substituted porphyrins. J. Am. Soc. Mass Spectrom. 25, 18–29. https://doi.org/10.1007/s13361-013-0750-6.

Montalbetti, N., Simonin, A., Dalghi, M.G., Kovacs, G., Hediger, M.A., 2014. Development and validation of a fast and homogeneous cell-based fluorescence screening assay for divalent metal transporter 1 (dmt1/slc11a2) using the FLIPR tetra. J. Biomol. Screen. 19, 900–908. https://doi.org/10.1177/1087057114521663.

Ng, D.C.H., Bao, H.L., Cheh, P.L., Huang, G., Zhang, T., Poli, V., Cao, X., 2006. Stat3 regulates microtubules by antagonizing the depolymerization activity of stathmin. J. Cell Biol. 172, 245–257. https://doi.org/10.1083/jcb.200503021.

Ng, J.Y., Chua, M.L., Zhang, C., Hong, S., Kumar, Y., Gokhale, R., Ee, P.L.R., 2020. *Chlorella vulgaris* extract as a serum replacement that enhances mammalian cell growth and protein expression. Front. Bioeng. Biotechnol. 8, 564667. https://doi.org/10.3389/fbioe.2020.564667.

Niu, Y., Pan, Y., Wang, Y., Qin, H., Fu, Y., Zhou, M., Kang, L., 2025. Ferroptosis induced by Pb exposure causes Parkinson's disease-related dopaminergic neuronal death. Environ. Sci. Technol. 59, 25186–25199. https://doi.org/10.1021/acs.est.5c11674.

Nothias, L.F., Petras, D., Schmid, R., Dührkop, K., Rainer, J., Sarvepalli, A., Protsyuk, I., Ernst, M., Tsugawa, H., Fleischauer, M., Aicheler, F., Aksenov, A.A., Alka, O., Allard, P.M., Barsch, A., Cachet, X., Caraballo-Rodriguez, A.M., Da Silva, R.R., Dang, T., Garg, N., Gauglitz, J.M., Gurevich, A., Isaac, G., Jarmusch, A.K., Kameník, Z., Kang, K.B., Kessler, N., Koester, I., Korf, A., Le Gouellec, A., Ludwig, M., Martin H, C., McCall, L.I., McSayles, J., Meyer, S.W., Mohimani, H., Morsy, M., Moyne, O., Neumann, S., Neuweger, H., Nguyen, N.H., Nothias-Esposito, M., Paolini, J., Phelan, V.V., Pluskal, T., Quinn, R.A., Rogers, S., Shrestha, B., Tripathi, A., van der Hooft, J.J.J., Vargas, F., Weldon, K.C., Witting, M., Yang, H., Zhang, Z., Zubeil, F., Kohlbacher, O., Böcker, S., Alexandrov, T., Bandeira, N., Wang, M., Dorrestein, P.C., 2020. Feature-based molecular networking in the GNPS analysis environment. Nat. Methods 17, 905–908. https://doi.org/10.1038/s41592-020-0933-6.

Ouyang, S., Li, H., Lou, L., Huang, Q., Zhang, Z., Mo, J., Li, M., Lu, J., Zhu, K., Chu, Y., Ding, W., Zhu, J., Lin, Z., Zhong, L., Wang, J., Yue, P., Turkson, J., Liu, P., Wang, Y., Zhang, X., 2022. Inhibition of STAT3-ferroptosis negative regulatory axis suppresses tumor growth and alleviates chemoresistance in gastric cancer. Redox Biol. 52, 102317. https://doi.org/10.1016/j.redox.2022.102317.

Pantami, H.A., Bustamam, M.S.A., Lee, S.Y., Ismail, I.S., Faudzi, S.M.M., Nakakuni, M., Shaari, K., 2020. Comprehensive GCMS and LC-MS/MS metabolite profiling of *Chlorella vulgaris*. Mar. Drugs 18, 367. https://doi.org/10.3390/MD18070367.

Payne, J.C., Ter Horst, M.A., Godwin, H.A., 1999. Lead fingers: Pb^{2+} binding to structural zinc-binding domains determined directly by monitoring lead-thiolate charge-transfer bands. J. Am. Chem. Soc. 121, 6850–6855. https://doi.org/10.1021/ja990899o.

Rădulescu, A., Lundgren, S., 2019. A pharmacokinetic model of lead absorption and calcium competitive dynamics. Sci. Rep. 9, 14225. https://doi.org/10.1038/s41598-019-50654-7.

Ravikumar, B., Sarkar, S., Davies, J.E., Futter, M., Garcia-Arencibia, M., Green-Thompson, Z.W., Jimenez-Sanchez, M., Korolchuk, V.I., Lichtenberg, M., Luo, S., Massey, D.C.O., Menzies, F.M., Moreau, K., Narayanan, U., Renna, M., Siddiqi, F.H., Underwood, B.R., Winslow And, A.R., Rubinsztein, D.C., 2010. Regulation of mammalian autophagy in physiology and pathophysiology. Physiol. Rev. 90, 1383–1435. https://doi.org/10.1152/physrev.00030.2009.

Re, R., Pellegrini, N., Proteggente, A., Pannala, A., Yang, M., Rice-Evans, C., 1999. Antioxidant activity applying an improved ABTS radical cation decolorization assay. Free Radic. Biol. Med. 26, 1231–1237. https://doi.org/10.1016/s0891-5849(98)00315-3.

Rosell-Melé, A., Carter, J.F., Maxwell, J.R., 1999. Liquid chromatography/tandem mass spectrometry of free base alkyl porphyrins for the characterization of the macrocyclic substituents in components of complex mixtures. Rapid Commun. Mass Spectrom. 13, 568–573. https://doi.org/10.1002/(SICI)1097-0231(19990415)13:7<568::AID-RCM525>3.0.CO;2-J.

Sanders, T., Liu, Y., Buchner, V., Tchounwou, P.B., 2009. Neurotoxic effects and biomarkers of lead exposure: a review. Rev. Environ. Healt. 24, 15–45. https://doi.org/10.1515/reveh.2009.24.1.15.

Schilling, K., Ujueta, F., Gao, S., Anderson, W.A., Escolar, E., Mon, A., Navas-Acien, A., Lamas, G.A., 2025. Pharmacokinetics of metal excretion following different doses of sodium EDTA infusion. Metallomics 17, mfaf010. https://doi.org/10.1093/mtomcs/mfaf010.

Schmid, R., Heuckeroth, S., Korf, A., Smirnov, A., Myers, O., Dyrlund, T.S., Bushuiev, R., Murray, K.J., Hoffmann, N., Lu, M., Sarvepalli, A., Zhang, Z., Fleischauer, M., Dührkop, K., Wesner, M., Hoogstra, S.J., Rudt, E., Mokshyna, O., Brungs, C., Ponomarov, K., Mutabdžija, L., Damiani, T., Pudney, C.J., Earll, M., Helmer, P.O., Fallon, T.R., Schulze, T., Rivas-Ubach, A., Bilbao, A., Richter, H., Nothias, L.F., Wang, M., Orešič, M., Weng, J.K., Böcker, S., Jeibmann, A., Hayen, H., Karst, U., Dorrestein, P.C., Petras, D., Du, X., Pluskal, T., 2023. Integrative analysis of multimodal mass spectrometry data in MZmine 3. Nat. Biotechnol. 41, 447–449. https://doi.org/10.1038/s41587-023-01690-2.

Sears, M.E., 2013. Chelation: harnessing and enhancing heavy metal detoxification - a review. Sci. World J. 13, 219840. https://doi.org/10.1155/2013/219840.

Shi, F., Yang, H., Sun, G., Cui, J., Li, Z., Wang, W., Zhang, Y., 2023. Pb induces ferroptosis in choroid plexus epithelial cells via Fe metabolism. Neurotox 95, 107–116. https://doi.org/10.1016/j.neuro.2023.01.005.

Sidbury, J.B., 1955. Lead poisoning; treatment with disodium calcium ethylenediamine-tetra-acetate. Am. J. Med. 18, 932–946. https://doi.org/10.1016/0002-9343(55)90174-1.

Song, X.B., Liu, G., Liu, F., Yan, Z.G., Wang, Z.Y., Liu, Z.P., Wang, L., 2017. Autophagy blockade and lysosomal membrane permeabilization contribute to lead-induced nephrotoxicity in primary rat proximal tubular cells. Cell Death Dis. 8, e2863. https://doi.org/10.1038/cddis.2017.262.

Soria-Aguilar, M.D.J., Martínez-Luévanos, A., Sánchez-Castillo, M.A., Carrillo-Pedroza, F. R., Toro, N., Narváez-García, V.M., 2021. Removal of Pb(II) from aqueous solutions by using steelmaking industry wastes: effect of blast furnace dust's chemical composition. Arab. J. Chem. 14, 103061. https://doi.org/10.1016/j.arabjc.2021.103061.

Tang, D., Chen, X., Kang, R., Kroemer, G., 2021. Ferroptosis: molecular mechanisms and health implications. Cell Res. 31, 107–125. https://doi.org/10.1038/s41422-020-00441-1.

Tariq, A., Hong, J., Nasr-El-Din, H., 2017. Chelating Agents in Productivity Enhancement: a Review. Society of Petroleum Engineers, Oklahoma, USA, SPE-185097-MS (SPE). https://doi.org/10.2118/185097-MS.

Thakur, R., Singh, S., Chauhan, A., Kumar, P., Saini, R.V., Saini, A.K., 2025. Lead and arsenic toxicity: emerging mechanisms, immunotoxic effects, and future research perspectives. BioMetals 38, 1421–1445. https://doi.org/10.1007/s10534-025-00717-2.

Thomas, S., Bonchev, D., 2010. A survey of current software for network analysis in molecular biology. Hum. Genomics 4, 353–360. https://doi.org/10.1186/1479-7364-4-5-353.

Tripathi, S., Poluri, K.M., 2021. Heavy metal detoxification mechanisms by microalgae: insights from transcriptomics analysis. Environ. Pollut. 285, 117443. https://doi.org/10.1016/j.envpol.2021.117443.

Wang, Q., Zhao, L., Zhao, H., Liu, X., Gao, L., Cheng, N., Cao, W., 2019. Complexation of luteolin with lead (II): Spectroscopy characterization and theoretical researches. J. Inorg. Biochem. 193, 25–30. https://doi.org/10.1016/j.jinorgbio.2019.01.007.

Wittkopf, N., Pickert, G., Billmeier, U., Mahapatro, M., Wirtz, S., Martini, E., Leppkes, M., Neurath, M.F., Becker, C., 2015. Activation of intestinal epithelial Stat3 orchestrates tissue defense during gastrointestinal infection. PLoS One 10, e0118401. https://doi.org/10.1371/journal.pone.0118401.

Wu, J.Y., Tso, R., Teo, H.S., Haldar, S., 2023. The utility of algae as sources of high value nutritional ingredients, particularly for alternative/complementary proteins to improve human health. Front. Nutr. 10, 1277343. https://doi.org/10.3389/fnut.2023.1277343.

Xie, G., Peng, Z., Liang, J., Larabee, S.M., Drachenberg, C.B., Yfantis, H., Raufman, J.-P., 2022. Zinc finger protein 277 is an intestinal transit-amplifying cell marker and colon cancer oncogene. JCI Insight 7. https://doi.org/10.1172/jci.insight.150894.

Yadavalli, R., Ratnapuram, H., Motamarry, S., Reddy, C.N., Ashokkumar, V., Kuppam, C., 2020. Simultaneous production of flavonoids and lipids from *Chlorella vulgaris* and *Chlorella pyrenoidosa*. Biomass Convers. Biorefin. 12, 683–691. https://doi.org/10.1007/s13399-020-01044-x/Published.

Yan, G., Dawood, M., Böckers, M., Klauck, S.M., Fottner, C., Weber, M.M., Efferth, T., 2020. Multiple modes of cell death in neuroendocrine tumors induced by artesunate. Phytomedicine 79, 153332. https://doi.org/10.1016/j.phymed.2020.153332.